Forward and Inverse Modelling of Atmospheric Nitrous Oxide Using MIROC4-Atmospheric Chemistry-Transport Model

Prabir K. PATRA

Research Institute for Global Change, JAMSTEC, Yokohama, Japan
Center for Environmental Remote Sensing, Chiba University, Chiba, Japan

Edward J. DLUGOKENCKY

Global Monitoring Laboratory, National Oceanic & Atmospheric Administration (NOAA), Colorado, USA

James W. ELKINS, Geoff S. DUTTON

Global Monitoring Laboratory, National Oceanic & Atmospheric Administration(NOAA), Colorado, USA
University of Colorado, Cooperative Institute for Research in Environmental Sciences, Colorado, USA

Yasunori TOHJIMA, Motoki SASAKAWA, Akihiko ITO

Earth System Division, National Institute for Environmental Studies, Tsukuba, Japan

Ray F. WEISS, Manfredi MANIZZA

Scripps Institution of Oceanography, University of California, California, USA

Paul B. KRUMMEL

CSIRO Oceans and Atmosphere, Australia

Ronald G. PRINN

Massachusetts Institute of Technology, Massachusetts, USA

Simon O'DOHERTY

School of Chemistry, University of Bristol, UK

Daniele BIANCHI

Atmospheric & Oceanic Sciences, University of California, California, USA

Cynthia NEVISON

Institute of Arctic and Alpine Research, University of Colorado, Colorado, USA

Corresponding author: Prabir K. Patra, Research Institute for Global Change, Japan Agency for Marine-Earth Science and Technology (JAMSTEC), 3173-25 Showa-machi, Kanazawa-ku, Yokohama, 236-0001, Japan
E-mail: prabir@jamstec.go.jp.

Efisio SOLAZZO

Unisystems Information Technologies, Belgium

Haeyoung LEE, Sangwon JOO

National Institute of Meteorological Sciences, South Korea

Eric A. KORT

Climate and Space Sciences and Engineering, University of Michigan, Michigan, USA

Suman MAITY and Masayuki TAKIGAWA

Research Institute for Global Change, JAMSTEC, Yokohama, Japan

Abstract

Atmospheric nitrous oxide (N_2O) contributes to global warming and stratospheric ozone depletion, so reducing uncertainty in estimates of emissions from different sources is important for climate policy. In this study, we simulate atmospheric N_2O using an atmospheric chemistry-transport model (ACTM), and the results are first compared with the in situ measurements. Five combinations of known (a priori) N_2O emissions due to natural soil, agricultural land, other human activities, and sea–air exchange are used. The N_2O lifetime is 127.6 ± 4.0 yr in the control ACTM simulation (range indicates interannual variability). Regional N_2O emissions are optimized using Bayesian inverse modeling for 84 partitions of the globe at monthly intervals, using measurements at 42 sites around the world covering 1997–2019. The best estimated global land and ocean emissions are 12.99 ± 0.22 TgN yr^{-1} and 2.74 ± 0.27 TgN yr^{-1}, respectively, for 2000–2009, and 14.30 ± 0.20 TgN yr^{-1} and 2.91 ± 0.27 TgN yr^{-1}, respectively, for 2010–2019. On regional scales, we find that the most recent ocean emission estimation, with lower emissions in the Southern Ocean regions, fits better with that predicted by the inversions. Marginally higher (lower) emissions than the inventory/model for the tropical (extratropical) land regions are estimated and validated using independent aircraft observations. Global land and ocean emission variabilities show a statistically significant correlation with El Niño Southern Oscillation (ENSO). Analysis of regional land emissions shows increases over America (Temperate North, Central, and Tropical), Central Africa, and Asia (South, East, and Southeast) between the 2000s and 2010s. Only Europe as a whole recorded a slight decrease in N_2O emissions due to the chemical industry. Our inversions suggest revisions to seasonal emission variations for three of the 15 land regions (East Asia, Temperate North America, and Central Africa), and the Southern Ocean region. The terrestrial ecosystem model (Vegetation Integrative SImulator for Trace Gases) can simulate annual total emissions in agreement with the observed N_2O growth rate since 1978, but the lag-time scales of N_2O emissions from nitrogen fertilizer application may need to be revised.

1. Introduction

Nitrous oxide (N_2O) emissions cause 300 times more warming over 100 years than equal emissions of carbon dioxide (CO_2), and N_2O has the 3rd largest increase in radiative forcing from 1750 to 2019 (Etminan et al. 2016; IPCC 2013). N_2O is inert in the troposphere and is dissociated by ultraviolet radiation (wavelength < 240 nm) and by reaction with oxygen in an excited state (O^1D) in the stratosphere where it plays the most significant role in ozone depletion (Crutzen and Ehhalt 1977; Fahey et al. 2018; Ravishankara et al. 2009). Because of natural emissions in the pre-industrial era (circa 1750), atmospheric N_2O was 271 ppb (parts per billion) (MacFarling Meure et al. 2006). Atmospheric N_2O averaged 327.5 ± 2.9 ppb from 2010 to 2019 (https://gml.noaa.gov/ccgg/trends_n2o), a 21 % increase from the pre-industrial level due to an increase in anthropogenic activities (Crippa et al. 2020; Ishijima et al. 2007). Of this 21 % N_2O increase, 18 % has occurred since 1900 with a large-scale application of nitrogen fertilizer. Natural production of N_2O dominantly occurs in soil, where bacteria fix nitrogen from the atmosphere, and bacteria-mediated geochemical processes in the ocean, both involving nitrification and denitrification in anoxic environments (Butterbach-Bahl et al. 2013; Yoshida et al. 1989).

A recent study showed large differences between atmospheric N_2O inversion estimates of emissions and process-based terrestrial ecosystem models for land and ocean regions and a large gap in land–ocean partitioning of N_2O emissions (Tian et al. 2020). The authors estimated emissions of 5.1 (range: 3.1–7.2) TgN yr^{-1} from global oceans and 10.8 (range: 9.3–12.5) TgN yr^{-1} from global land for 2000–2009 by inverse (top-down) modeling, and bottom-up global total emission of 16.4 (range: 12.3–22.4) TgN yr^{-1}. Bottom-up emission estimations are based on inventory emissions for various activity sectors and process modeling of terrestrial and ocean biogeochemical cycles (Bouwman et al. 2013; Buitenhuis et al. 2018; Butterbach-Bahl et al. 2013; Ito 2019; Winiwarter et al. 2018). Over the past few decades, large and systematic efforts have resulted in an evolution of sea–air N_2O emission distribution based on oceanic pN_2O up-scaling and empirical modeling (Manizza et al. 2012; Nevison at al. 1995; Yang et al. 2020), which have not yet been utilized in an inverse modeling framework for understanding their impacts on estimated N_2O emissions at global and regional scales. The inverse models generally under-determined the emissions because of the lack of sufficient high-quality measurements to constrain regional N_2O emissions and because of the uncertainties in parameterizations of photochemical loss and atmospheric tracer transport in the forward-running atmospheric chemistry-transport models (ACTMs). One long-standing challenge remains in simulating N_2O seasonal cycles at most of the in situ measurement sites (Nevison et al. 2007; Ricaud et al. 2021; Thompson et al. 2014a).

Regional emissions by inverse modeling of atmospheric N_2O were estimated in the past 15 years because of improvements in measurement precision and development of long-term measurement networks (Hirsch et al. 2006; Huang et al. 2008; Saikawa et al. 2014; Thompson et al. 2019; Wilson et al. 2014) and improvements in, and proliferation of, top-down models (Ishijima et al. 2010; Prather et al. 2015; Thompson et al. 2014b, c, 2019). Thompson et al. (2019) is the first study to explore the role of a priori emissions and chemistry-transport models on the estimated N_2O emissions by inversion. Nevertheless, no study has been conducted to elucidate the roles of these factors on the estimated emission in a single modeling system, to disentangle the roles of selecting a priori emissions, and processes in forward-running ACTMs. An emission assessment framework using multi-model inversion provides only the range of uncertainty arising from their own choices of transport, chemistry, and emissions but does not elucidate the sources of uncertainty. The quality assessment of the ACTM simulations is one of the key factors to enable better estimates of trace gas sources and sinks at Earth's surface via inverse modeling (Rayner 2021).

Here, we use the JAMSTEC's Model for Interdisciplinary Research on Climate (MIROC, version 4.0) (Watanabe et al. 2011)-based atmospheric chemistry-transport model (referred to as MIROC4-ACTM) for simulating N_2O and subsequently performed inverse modeling for 84 partitions of the globe (Ishijima et al. 2010; Patra et al. 2018; Thompson et al. 2019). The sensitivity of the estimated N_2O emissions is discussed in relation to the ACTM transport and chemistry parameterizations, selection of a priori emission scenarios, and choices of prior emission and measurement data uncertainties in the inverse model. The study significantly differs from the MIROC4-ACTM inversion used in Thompson et al. (2019), for the choices of a large number of a priori emission scenarios, input parameter selection for the inverse model, and ACTM transport sensitivity simulations.
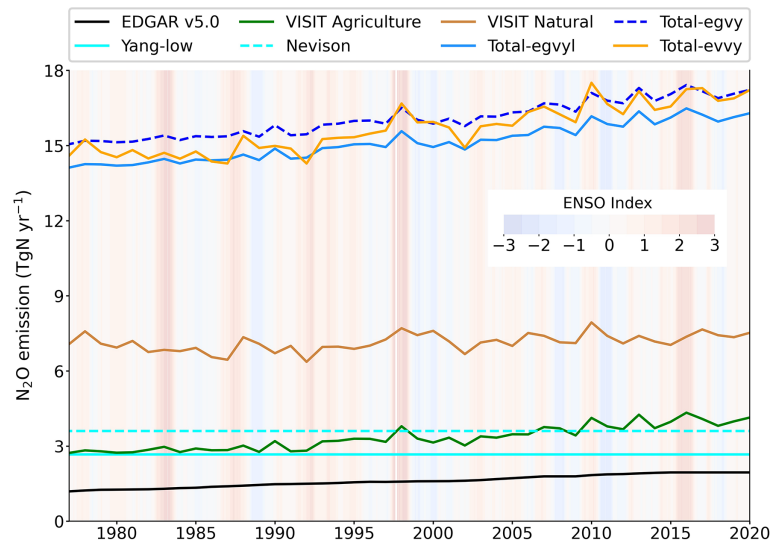
Fig. 1. Time series of N_2O fluxes using three ocean fluxes (scaled to light blue lines; Table 1) and two land fluxes due to anthropogenic fluxes (GEIA and VISIT in Total-egvy and Total-evvy, respectively) and a set of industrial emissions (EDGARv5.0). The ENSO cycle is depicted as the colored shading (Wolter and Timlin 2011) (data source: Multivariate ENSO Index Version 2 (MEI.v2); https://psl.noaa.gov/enso/mei/).

2. Data and methods

2.1 A priori N_2O fluxes from land and ocean

Four main sources contribute to total N_2O emissions, namely, 1) anthropogenic sources from industrial activities, 2) emissions from natural soils, 3) emissions from fertilized/agricultural soils, and 4) sea–air fluxes.

The Emissions Database for Global Atmospheric Research, version 5.0 (EDGAR_v5.0) is an inventory-based estimate of emissions from industrial activities, covering energy production and use, manufacturing and construction, transport, direct and indirect emissions from manure management, emissions from biomass burning, direct and indirect emissions from managed soils, and treatment of solid waste and wastewater (Crippa et al. 2020). EDGAR presents emissions for the three main greenhouse gases (fossil CO_2, CH_4, and N_2O) and F-gases. The emissions are calculated by using sectorial activity data supplied by different institutions, and emission factors generally derived from IPCC guidelines (IPCC 2006; Eggleston et al. 2006). Considering the consistent methodology for emission estimation, the EDGAR database assures a full cross-country comparability (Oreggioni et al. 2021). Uncertainties of the EDGAR_v5.0 emissions are detailed for all greenhouse gases (Solazzo et al. 2021). For N_2O particularly, the global uncertainties stemming from agricultural activities were greater than 200 %. Figure 1 shows that global total industrial emissions in EDGAR_v5.0 amounted to 1.34 ± 0.07, 1.54 ± 0.04, 1.70 ± 0.08 and 1.92 ± 0.04 TgN yr^{-1} in the 1980s, 1990s, 2000s, and 2010s, respectively.

In one set of simulations, natural soil emissions were maintained constant at 7.5 TgN yr^{-1} for the whole period of simulation, for which 1×1 degree gridded emissions are taken from the Global Emissions InitiAtive (GEIA) database (Bouwman et al. 2013). Natural soil emissions are also taken from a terrestrial ecosystem model–Vegetation Integrative SImulator for Trace Gases (VISIT) (Ito et al. 2018). The VISIT model simulates emissions of N_2O from natural soil using a generalized scheme of nitrification and denitrification (Parton et al. 1996), in which the fraction of N_2 and N_2O emissions varies dynamically dependent on soil temperature and moisture conditions. Also, the N_2O emission is dependent on soil nitrogen concentration, which is affected by various processes such as atmospheric deposition, nitrate leaching, and human fertilizer input. The result shows interannual variations with relatively high values in El Niño years but remained fairly stable at 7.1 ± 0.3 TgN yr^{-1} during 1980–2019 (Fig. 1). Agricultural soil N_2O emissions are simulated using nitrogen fertilizer input data from the statistical database of the Food and Agriculture Organization of the United Nations (FAOSTAT; https://www.fao.org/faostat/en/#data/RFN), which

Table 1. List of forward simulations cases (left column), which have used different combinations of 4 surface emission types (column 2–5). Global totals (right column) for the two nearest decades are given in TgN yr^{-1}. The a priori emission distributions for the cases evvy, egvm and egvn are shown in Section 3.1, where all distinct ocean (3) and land (2) flux maps can be found.

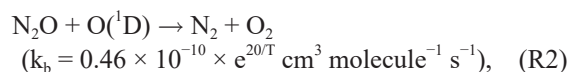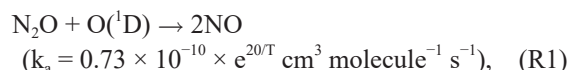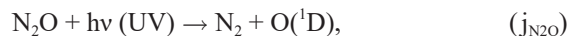| Abbreviated name	Industrial emissions	Natural soil emissions	Agricultural soil emissions	Ocean/sea-air exchange	Global totals 2000s, 2010s
egvy	EDGAR v5.0	GEIA	VISIT	Yang–scaled	16.27, 17.06
egvyl	EDGAR v5.0	GEIA	VISIT	Yang–low	15.34, 16.13
egvm	EDGAR v5.0	GEIA	VISIT	Manizza–scaled	16.15, 16.95
egvn	EDGAR v5.0	GEIA	VISIT	Nevison	16.25, 17.05
evvy	EDGAR v5.0	VISIT	VISIT	Yang–scaled	15.89, 16.84

showed steady increases, with 2.84 ± 0.10, 3.20 ± 0.28, 3.40 ± 0.22, and 3.97 ± 0.23 TgN yr^{-1} in the 1980s, 1990s, 2000s, and 2010s, respectively (Fig. 1).

Sea–air fluxes are taken from three different sources and have evolved dramatically since the mid-1990s. Nevison et al. (1995) estimated global total emissions of 3.6 TgN yr^{-1} by globally extrapolating 60,000 partial pressure difference (ΔpN_2O) measurements between air and seawater with limited seasonal and spatial coverage. These were paired with air–sea transfer coefficients using modeled windspeeds that were considered biased high over the Southern Ocean. Manizza et al. (2012) modeled oceanic N_2O cycling in a physical–biogeochemical model, which accounts for biogeochemical tracers (PO_4, SiO_2, O_2, DIC, alkalinity, and iron) in an ecosystem component based on two phytoplankton groups (diatoms and small phytoplankton) and one generic grazing zooplankton (Dutkiewicz et al. 2005). The air–sea gas fluxes of N_2O were calculated according to wind speed-dependent gas transfer velocity (Wanninkhof 1992), generating a net outgassing flux of 4.5 TgN yr^{-1}. The net outgassing flux is scaled to a global total value of 3.52 TgN yr^{-1} for this analysis. More recently, Yang et al. (2020) used the most comprehensive database of surface ΔpN_2O measurements (over 158,000 in total) to extrapolate observations to the global ocean with a machine learning ensemble approach; together with revised estimates of gas transfer velocity, the study and produced a much different flux map (details in the results section) and global total emissions at 4.2 ± 1.0 TgN yr^{-1}. Yang et al. (2020) fluxes are scaled to 3.6 TgN yr^{-1} and 2.67 TgN yr^{-1} for two simulation cases, which are referred to as Yang-scaled and Yang-low, respectively (Table 1). This work was inspired by these recent developments in sea–air N_2O flux estimation because the recent modeling studies of atmospheric N_2O faced difficulty in choosing an ocean flux model (Thompson et al. 2019; Tian et al. 2020).

2.2 JAMSTEC's MIROC4-ACTM

The MIROC4-ACTM was developed for the simulation of long-lived species (Patra et al. 2018). The MIROC4 atmospheric general circulation fields of horizontal winds (U, V) and temperature (T) are nudged to the Japanese 55-year reanalysis with Newtonian relaxation times of 1 day for U and V, and 5 days for T [control; referred to as "Prior (UV1,T5)"]. A sensitivity simulation is performed by weakening the nudging strength with Newtonian relaxation times of 5 days for U and V, and 10 days for T [WN; referred to as "Prior (UV5,T10)"].

Loss of N_2O due to photolysis by solar ultraviolet (UV) radiation and two paths for reaction with $O(^1D)$ is modeled in ACTM as follows:

$$N_2O + hv\ (UV) \rightarrow N_2 + O(^1D), \qquad (j_{N2O})$$

$$N_2O + O(^1D) \rightarrow 2NO$$
$$(k_a = 0.73 \times 10^{-10} \times e^{20/T}\ cm^3\ molecule^{-1}\ s^{-1}), \quad (R1)$$

$$N_2O + O(^1D) \rightarrow N_2 + O_2$$
$$(k_b = 0.46 \times 10^{-10} \times e^{20/T}\ cm^3\ molecule^{-1}\ s^{-1}), \quad (R2)$$

where T is the air temperature and k_a and k_b are the rate constants for the chemical loss reactions (R1, R2). The reaction rate constants are taken from the Jet Propulsion Laboratory (JPL) synthesis report (Sander et al. 2011). The N_2O photolysis rate (j_{N2O}) is calculated from the temperature-dependent absorption cross-sections at three wavelength bands of 185–200, 200–230, and 230–278 nm (Ishijima et al. 2010), which are averaged from the JPL publication 10-6, evaluation number 17 (Sander et al. 2011). The solar UV flux at different layers of the atmosphere is calculated using the radiation package termed "mstrnX" that computes radiation fluxes and heating rates, which agree well with those calculated by line-by-line radiation scheme HITRAN2004 (Sekiguchi and Nakajima 2008). A climatological 11 year solar cycle is introduced. The concentration of $O(^1D)$ is calculated online from a
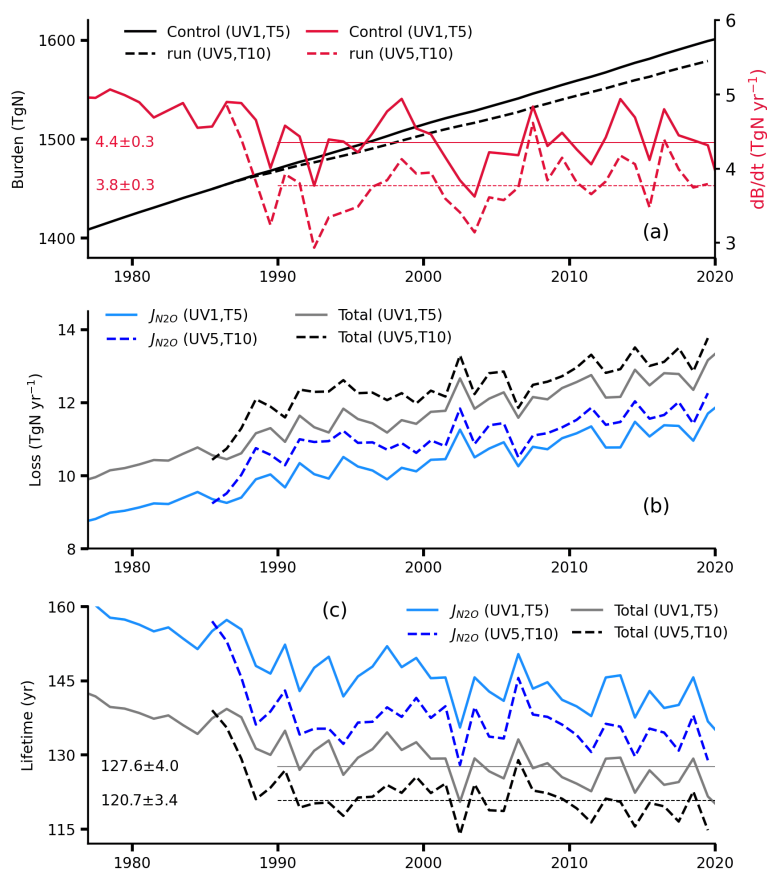
Fig. 2. Time evolution of N_2O in the global atmosphere of MIROC4-ACTM; burden and rate of burden change (a), loss rates (b), and lifetimes (c). These calculations are based on the simulation using emission case evvy (ref. Fig. 1). Simulations are shown for control and sensitivity (weak nudging—WN) transport cases. The atmospheric N_2O burden to concentration ratio is estimated to be 4.785 ± 0.005 Tg ppb^{-1}.

climatological ozone distribution, and the ozone photolysis rates in the stratosphere (Takigawa et al. 1999).

Figure 2 shows the MIROC4-ACTM simulated atmospheric burden (B) and burden change rate, loss rates due to j_{N2O} alone and the sum (L) of j_{N2O} + R1 + R2, and photochemical lifetimes (= B/L). The control transport simulation captures well the long-term measurements from the National Oceanic and Atmospheric Administration (NOAA) Global Monitoring Laboratory, and the Advanced Global Atmospheric Gases Experiment (AGAGE) networks (Fig. 3). The mean atmospheric lifetime of N_2O in the MIROC4-ACTM is 127.6 ± 4.0 yr for 1990–2019, which is within the range of the IPCC recommended value of 118–131 yr (Huang et al. 2008; IPCC 2013), and agrees well with the Stratosphere–troposphere Processes And their Role in Climate (SPARC) recommended steady-state lifetime of 123 yr, most likely range 104–152 yr (Ko

et al. 2013). In the MIROC4-ACTM transport sensitivity simulation (UV5,T10), N_2O lifetime is shortened to 120.7 ± 3.4 yr as the transport barrier around the tropopause region is relaxed and the northern polar jet strengthened which enabled faster transport of mass into the middle to upper troposphere (supplementary materials, Fig. S1). However, a comparison with balloon-borne cryosampling experiments covering the altitudes of 8–37 km cannot unambiguously confirm the accuracy of the nudging strength (Fig. S2). The model transport uncertainty will be addressed later in the article using SF_6 simulations.

The lifetime of N_2O has large implications for the estimation of global (and regional) emissions by inverse modeling. A simple calculation suggests that, if the lifetime is shortened by approximately 7 years, the global total N_2O emission is required to increase by approximately 0.6 TgN yr^{-1} (ref. Eq. 1 below). Hence,
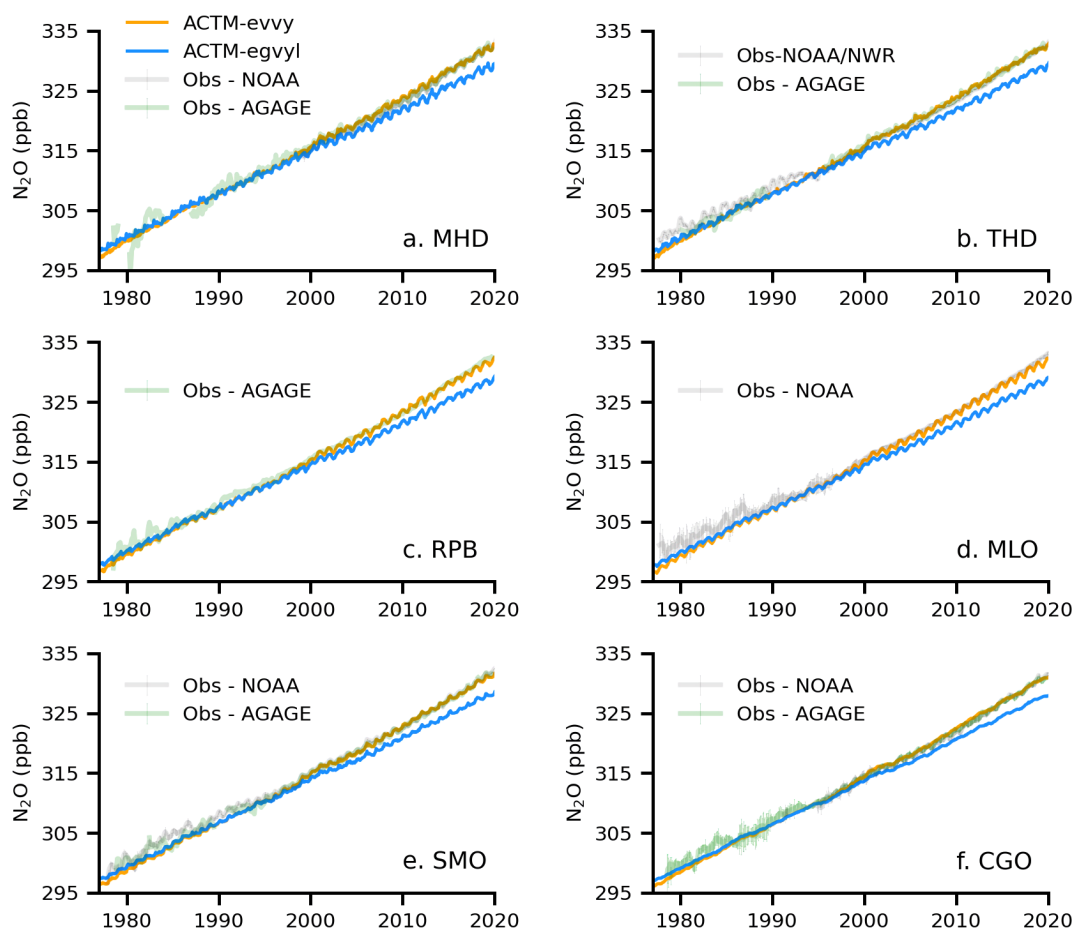
Fig. 3. Example time series of N$_2$O from AGAGE and NOAA sites, where measurements have been conducted since the late 1970s. Note the common legends for model simulations (top-left panel). Only two model simulations are shown here for clarity, the best case for growth rate (ACTM-evvy) and the one with the slowest growth rate (ACTM-egvyl). The other three simulations, as listed in Table 1, differ in growth rates as expected from their global total emissions.

inversion estimated emissions would spread as much as 1.1 TgN yr^{-1} using the ACTMs with mean N$_2$O lifetime covering the IPCC (2013) recommended range.

$$d(B_{CTL} - B_{WN}) = (E - E) - (B_{CTL}/\tau_{CTL} - B_{WN}/\tau_{WN}),$$

$$0.6 \text{ (simulated)} = -(1537.5/127.6 - 1523.0/120.7)$$

$$= -12.05 + 12.62 = 0.6. \quad (1)$$

2.3   N$_2$O observations

The N$_2$O observations are reported in units of dry-air mole fraction in parts per billion (nmol mol^{-1}, ppb). Supplementary Table S1 provides the full list and location details of 42 measurement sites used in inverse modeling. We have used 35 NOAA flask-air sampling sites (Dlugokencky et al. 1994), five AGAGE

high-frequency real-time measurement sites (Prinn et al. 2018), and two NIES high-frequency real-time measurement sites (Tohjima et al. 2000). Measurement calibration scales are adjusted to fit with the more dense observation network of NOAA for inverse model calculation. The AGAGE measurement scale (SIO-16) is higher by 0.55 ppb, and the NIES measurement scale (NIES-96) lower by 0.65 ppb, when compared with the NOAA-2006A scale, which was adopted by the World Meteorological Organization Global Atmosphere Watch program (GAW) as the GAW N$_2$O standard scale (Hall et al. 2007). It is worth mentioning here that we could fairly successfully derive these scale offsets, +0.57 ppb and −0.72 ppb, respectively, for AGAGE and NIES data relative to

NOAA by performing an inversion (methodology below) without applying the scale adjustments. The inversion estimated scale offset between NOAA and AGAGE is in better agreement with the NOAA-2006A and SIO-16 scales because of several overlapping sites (Mace Head—MHD, Republic of Barbados—RPB, Samoa Observatory—SMO, and Cape Grim Observatory—CGO), whereas the NIES sites are unique from the NOAA network and inversion estimated scale offset comprises bias corrections by inversion and measurement scale difference. We also used continuous N_2O data from Anmyeondo (AMY), a WMO/GAW site (126.32°E, 36.53°N, 47 m), which are reported at NOAA-2006A scale. This station is located in the west part of South Korea and the airmass is affected by local/regional/long-range transport (Lee et al. 2019).

Because of data availability at only a small number (< 10) sites before 1996 and after 2020, we decided to perform inverse model simulation of N_2O only for 1996–2020 so that the global and regional emissions can be analyzed for 1997–2019 after discarding the first and the final years as inversion spin-up and spin-down years. The new measurement systems since the mid-1990s have also improved the measurement precision (Fig. 3) and greatly increased observational network coverage following the analysis of weekly air samples from NOAA's cooperative global air sampling network. A historical perspective of N_2O measurements is given in the Supplementary Material. The MIROC4-ACTM simulation using newly developed emission estimations (EDGARv5.0, VISIT, Ocean) enabled us to simulate the N_2O measurements since the late 1970s. The average model–observation difference for any given year is within approximately 1 ppb at the longest-serving N_2O measurement sites of the AGAGE and NOAA HATS programs, when compared with the ACTM-evvy simulation case. The ACTM-egvyl case using lower emissions from Yang et al. (2020) underestimates the N_2O growth rate (blue line in Fig. 3). The simulations (ACTM-egvn/egvm/egvy) using GEIA natural soil emissions overestimate N_2O growth rate in the years before 1996 (not shown), because of higher global totals compared with that using VISIT natural soil emissions (ref. Fig. 1).

2.4 Curve fitting and filling data gaps

We have used a curve fitting software that uses harmonic fitting and Butterworth digital filter, which enables us to derive fitted curve and long-term trend lines (Nakazawa et al. 1997). The time derivative of the long-term trends gives N_2O growth rates and the differences of the monthly mean data or fitted line

from those long-term trend lines give N_2O seasonal cycles (Fig. 4). We fit both the measured and model time series at daily–weekly time intervals with six harmonics and by setting a cutoff length of 24 months for the digital filter. We also calculate monthly mean residual standard deviations (RSDs) from the differences between measured and fitted data (error bars in Fig. 4, upper row). The RSDs are used as a measure of the difficulty for the coarse spatial-resolution global ACTMs to simulate N_2O at the observation sites and were used to weight the measurement data for inverse model derived flux estimates (next section). The N_2O growth rates are generally higher during the La Niña phase (blue shade) and lower during the El Niño phase (red shade) of the ENSO cycle (Fig. 4, lower row) (Ishijima et al. 2009). Statistically significant correlations for ENSO and N_2O growth rates are found for the EIC, −0.35 and −0.40 for observed and ACTM-evvy, respectively, because the site is located in the area under strong ENSO influence. Phases of the two simulations are in good agreement with each other, except for the small differences arising from the oceanic emission distributions and their transport, and systematically lower growth rate is simulated for egvyl compared with egvn emission case because of lower global totals.

2.5 Inverse modeling of regional fluxes

The source strengths are predicted by the least squares solution of the model–measurement differences, by assuming linear relations between regional emission matrix (S) and model–measurement difference matrix (D), which are defined by the Green's function (G) using unitary regional source to concentration change relationships. The following equations are used to predict optimized (inversion) sources and associated source error covariance matrices (Cs):

$$S = S_0 + (G^T C_D^{-1} G + C_{S_0}^{-1})^{-1} G^T C_D^{-1} (D_{Obs} - D_{ACTM}), \quad (2)$$
$$C_S = (G^T C_D^{-1} G + C_{S_0}^{-1})^{-1}, \quad\quad\quad\quad\quad (3)$$

where, S_0 = regional prior source matrix, C_{S_0} = prior source error covariance matrix (diagonal only), D_{Obs} = measurement data matrix, D_{ACTM} = chemistry-transport model simulations using a priori emissions, and C_D = measurement data error covariance matrix. We abbreviate prior flux uncertainty (PFU) and measurement data uncertainty (MDU), which are calculated as the square root of C_{S_0} and C_D, respectively.

The G matrix is prepared by simulating monthly and unitary emissions from 84 partitions of the globe (Fig. 5a) and sampling the signals at the measurement sites (Fig. 5b). Each of these monthly pulse (84 × 12
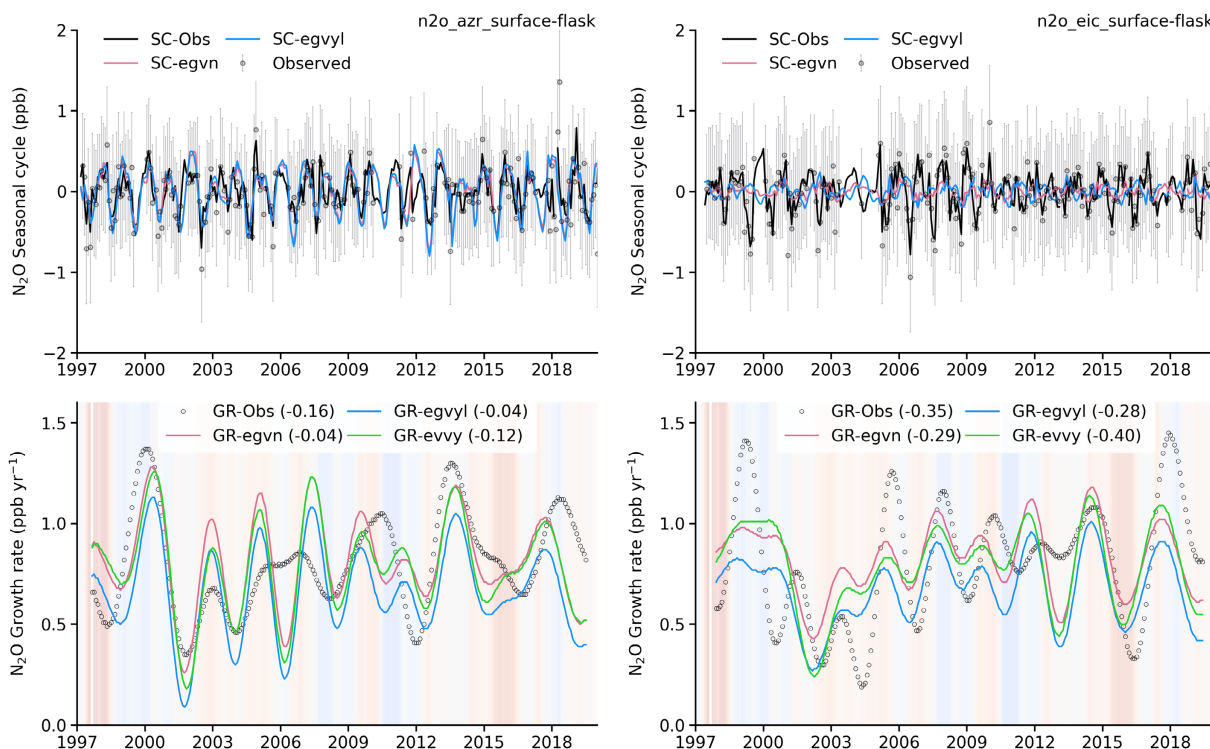
Fig. 4.   Seasonal cycles (SC: upper panels) and growth rates (GR: lower panels) of N_2O calculated using digital filtering from the time series at AZR (27.38°W, 38.77°N; left column) and EIC (109.43°W, 27.16°S; right column). The monthly mean RSDs are depicted as the error bars on the seasonal cycles (upper panels). The lower panels show growth rates (lines) and the ENSO cycle as the colored shading (ENSO and growth rate correlation coefficients are given within parenthesis in legends). These two sites are selected to show the advantages and limitations of data gap filling through the fitting and filtering method applied here.

= 1008) simulations are run for 47 additional months. Although D_{ACTM} is simulated using interannually varying winds, we have chosen to construct the G matrix for only 2011 to save computational resources, without compromising significantly the quality of inversion results for the estimation of the interannual emission variability (based on our sensitivity test for CO_2 inversions using for annually repeating and interannually varying G matrix; unpublished data). The PFU is assigned to each of the 84 regions by their regional total fluxes at monthly intervals (referred to as PFU_100 %). Additionally, for testing the stability of the inversion model setup, we have varied the regional PFU values as 25, 50, 200, and 400 % of their regional total fluxes. Table 2 shows the mean of PFUs for 84 regions. For the MDU, we have used the monthly varying RSDs for each station plus a constant value to account for the measurement accuracy (Table 2).

The seasonally varying MDUs for each site are calculated on the basis of a fixed term (representing instrumental uncertainty, in the range of 0.3–0.4 ppb) and a variable term to account for the site representation error corresponding to the coarse horizontal resolution of MIROC4-ACTM. The variable term is scaled from the RSDs of the measurement time series as defined in Section 2.4. Figure 6 shows the 2000–2019 mean values of MDUs in this study. Four different cases are implemented in our inversions, and labeled MDU_180 % ($\sqrt{0.2+RSD}$), MDU_152 % ($\sqrt{0.2+RSD\cdot0.5}$), MDU_93 % ($\sqrt{0.1+RSD\cdot0.3}$), and MDU_112 % ($\sqrt{0.1+RSD\cdot0.1}$). The %-values are calculated on the basis of the mean MDU with respect to the RSDs (Fig. 6). The square root values are used to dampen the high contrast in RSDs among the sites (a value–judgment).

In total, we have conducted 100 inversions (5 emissions × 5 PFUs × 4 MDUs) using control MIROC4-ACTM simulations, and the predicted emissions are analyzed here. The five emission cases are egvy, egvyl, egvm, egvn, and evvy (Table 1). To evaluate the good-
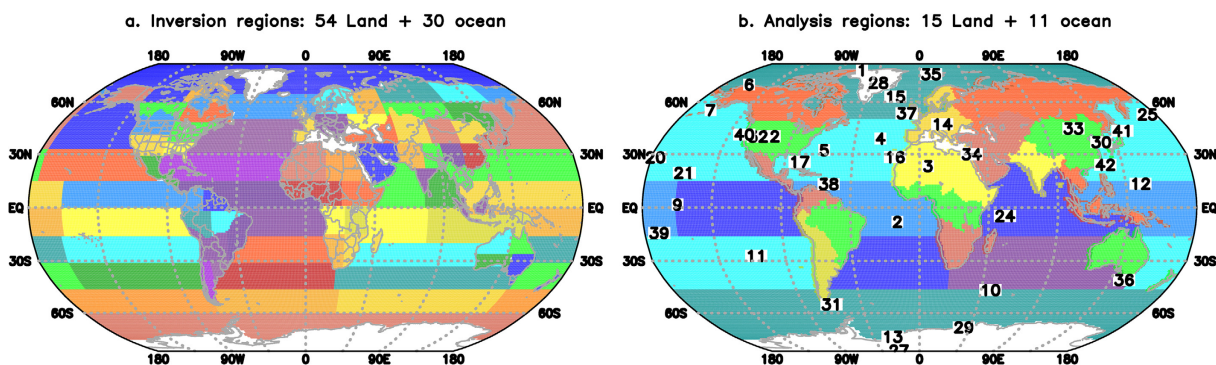
Fig. 5.　Division of 84 inversion regions (54 land and 30 ocean) (a), 26 analysis regions (15 land and 11 ocean) along with the 42 measurement sites used in the inversions (b). Table S1 provides a detailed list of the measurement sites.

Table 2.　Values of χ^2 for the inversion cases which are run by changing PFU and MDU for the ACTM-evvy forward simulation only.

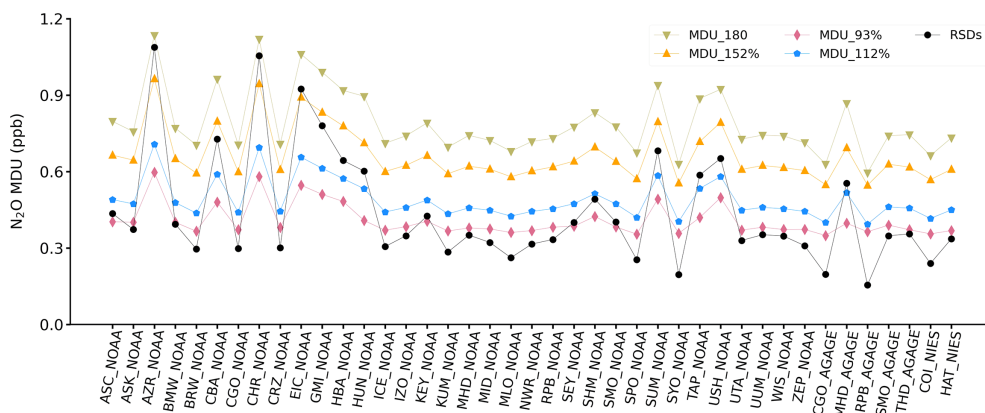| evvy case (regional mean PFU, TgN yr^{-1})	MDU_180 % $\sqrt{0.2+\mathrm{RSD}}$	MDU_152 % $\sqrt{0.2+\mathrm{RSD}\cdot 0.5}$	MDU_93 % $\sqrt{0.1+\mathrm{RSD}\cdot 0.3}$	MDU_112 % $\sqrt{0.1+\mathrm{RSD}\cdot 0.1}$
PFU_25 % (0.072)	0.35	0.47	1.13	0.80
PFU_50 % (0.144)	0.29	0.39	0.87 (best case)	0.62
PFU_100 % (0.288)	0.22	0.28	0.58	0.44
PFU_200 % (0.575)	0.15	0.19	0.38	0.30
PFU_400 % (0.152)	0.10	0.13	0.20	0.21

Fig. 6.　Measurement data uncertainties as used in the inversions (ref. Table 2) are shown for the 42 sites.

ness of fit, we used N_2O abundance and emission χ^2 = $[(D − D_{predicted})^2/C_D + (S − S_0)^2/C_S]$ for each of the inversions and the values for the ACTM-evvy case are shown in Table 2. The results suggest MDU_93 % and PFU_50 % (or PFU_25 %) produced the χ^2 values closest to 1, implying no overfitting to the measurement or too loose/strict PFU. Results of the other four emission cases yield similar χ^2 for MDU and PFU changes as in the case of evvy.

Table 3. Summary of the land and ocean total N_2O emissions due to the choices of prior flux uncertainty and measurement data uncertainty. The results are averaged over 5 forward model simulations (ref. Table 1) and the spread is given as 1-σ standard deviation.

	Global Land (TgN yr⁻¹)		Global Ocean		Global Land (TgN yr⁻¹)		Global Ocean	
	2000s	2010s	2000s	2010s	2000s	2010s	2000s	2010s
Prior emission								
	12.58 ± 0.35	13.41 ± 0.28	3.40 ± 0.41	3.40 ± 0.41				
Predicted emission, MDU_112 % $\sqrt{0.1+RSD\cdot0.1}$								
PFU_25 %	12.78 ± 0.24	14.09 ± 0.22	2.97 ± 0.29	3.10 ± 0.30				
PFU_50 %	13.07 ± 0.22	14.37 ± 0.20	2.65 ± 0.26	2.84 ± 0.26				
PFU_100 %	13.41 ± 0.21	14.68 ± 0.21	2.30 ± 0.25	2.56 ± 0.26				
PFU_200 %	13.69 ± 0.22	14.91 ± 0.23	2.02 ± 0.24	2.36 ± 0.26				
PFU_400 %	13.84 ± 0.23	14.98 ± 0.25	1.89 ± 0.24	2.32 ± 0.26				
Predicted emission, MDU_93 % $\sqrt{0.1+RSD\cdot0.3}$					Weakly nudged MIROC4-ACTM (UV5, T10)			
PFU_25 %	12.73 ± 0.25	14.04 ± 0.22	3.02 ± 0.30	3.14 ± 0.31	13.10 ± 0.25	14.42 ± 0.22	3.06 ± 0.30	3.19 ± 0.31
PFU_50 %	12.99 ± 0.22	14.30 ± 0.20	2.74 ± 0.27	2.91 ± 0.27	13.29 ± 0.21	14.59 ± 0.20	2.85 ± 0.26	3.04 ± 0.27
PFU_100 %	13.33 ± 0.21	14.60 ± 0.20	2.38 ± 0.25	2.63 ± 0.26	13.50 ± 0.22	14.79 ± 0.21	2.61 ± 0.26	2.87 ± 0.26
PFU_200 %	13.62 ± 0.22	14.85 ± 0.22	2.09 ± 0.25	2.41 ± 0.26	13.68 ± 0.22	14.95 ± 0.24	2.42 ± 0.26	2.73 ± 0.27
PFU_400 %	13.81 ± 0.22	14.97 ± 0.24	1.91 ± 0.24	2.32 ± 0.26	13.75 ± 0.25	14.99 ± 0.27	2.36 ± 0.26	2.71 ± 0.28
Predicted emission, MDU_152 % $\sqrt{0.2+RSD\cdot0.5}$					Predicted emission, MDU_180 % $\sqrt{0.2+RSD}$			
PFU_25 %	12.65 ± 0.27	13.97 ± 0.23	3.10 ± 0.32	3.20 ± 0.32	12.63 ± 0.27	13.93 ± 0.24	3.13 ± 0.33	3.22 ± 0.33
PFU_50 %	12.85 ± 0.23	14.17 ± 0.21	2.88 ± 0.28	3.03 ± 0.28	12.79 ± 0.24	14.11 ± 0.21	2.94 ± 0.29	3.08 ± 0.29
PFU_100 %	13.17 ± 0.21	14.47 ± 0.20	2.54 ± 0.26	2.75 ± 0.26	13.09 ± 0.21	14.39 ± 0.20	2.63 ± 0.26	2.82 ± 0.26
PFU_200 %	13.50 ± 0.21	14.76 ± 0.21	2.21 ± 0.25	2.49 ± 0.26	13.43 ± 0.21	14.69 ± 0.21	2.28 ± 0.25	2.54 ± 0.26
PFU_400 %	13.74 ± 0.22	14.94 ± 0.23	1.97 ± 0.24	2.34 ± 0.26	13.69 ± 0.22	14.90 ± 0.23	2.02 ± 0.24	2.37 ± 0.26

3. Results and discussion

Table 3 lists all inversion cases, by detailing the global total land and ocean total emissions for the decade of the 2000s (2000–2009) and the 2010s (2010–2019). The results for varying MDUs and PFUs are given as the ensemble mean and spread of five emission cases. As expected from the Bayesian inversion framework (Eqs. 2 and 3), the predicted emissions differ significantly from the prior emission when the MDUs are smaller, i.e., a greater impact of the observations on emission corrections ($S-S_0$). By contrast, the predicted emissions differ by a greater amount when the PFUs are increased, which relaxes the constraints on prior emissions, i.e., increases the effective degrees of freedom for emission correction. A dipole for the land–ocean emission partitioning is found for the low to high PFU. Global land emissions are greater for PFU_400 % than for PFU_25 %, with a compensating lower global ocean emission. Our best estimate ($\chi^2 = 0.87$) of global land and ocean emissions for MDU_93 % and PFU_50 % are 12.99 ± 0.22 TgN yr⁻¹ and 2.74 ± 0.27 TgN yr⁻¹, respectively,

for the 2000s, 14.30 ± 0.20 TgN yr⁻¹ and 2.91 ± 0.27 TgN yr⁻¹, respectively, for the 2010s. These values are in good agreement with the prior emissions when the model ensemble spreads are considered.

3.1 Global distributions of N_2O emissions

The latitude–longitude distributions of N_2O emissions show that prior emissions over the land between the five emission ensembles did not vary much; only one ensemble (evvy case; Fig. 7a) used different natural soil emissions from the VISIT model, whereas all others use emissions from the GEIA inventory. Conversely, we used four different oceanic emission cases (Table 1)—three varying in flux patterns (Figs. 7a–c for egvn, egvm, and egvy, respectively) and two for the global total emissions (egvy and egvyl). The predicted emission distributions suggest an increase in emissions over the tropical land regions relative to the prior emissions, whereas both the land and ocean regions of the middle–high latitudes are predicted to have lower emissions than the prior emissions (Figs. 7d–f). The predicted–prior emissions over land regions show similar patterns for all the ocean emis-
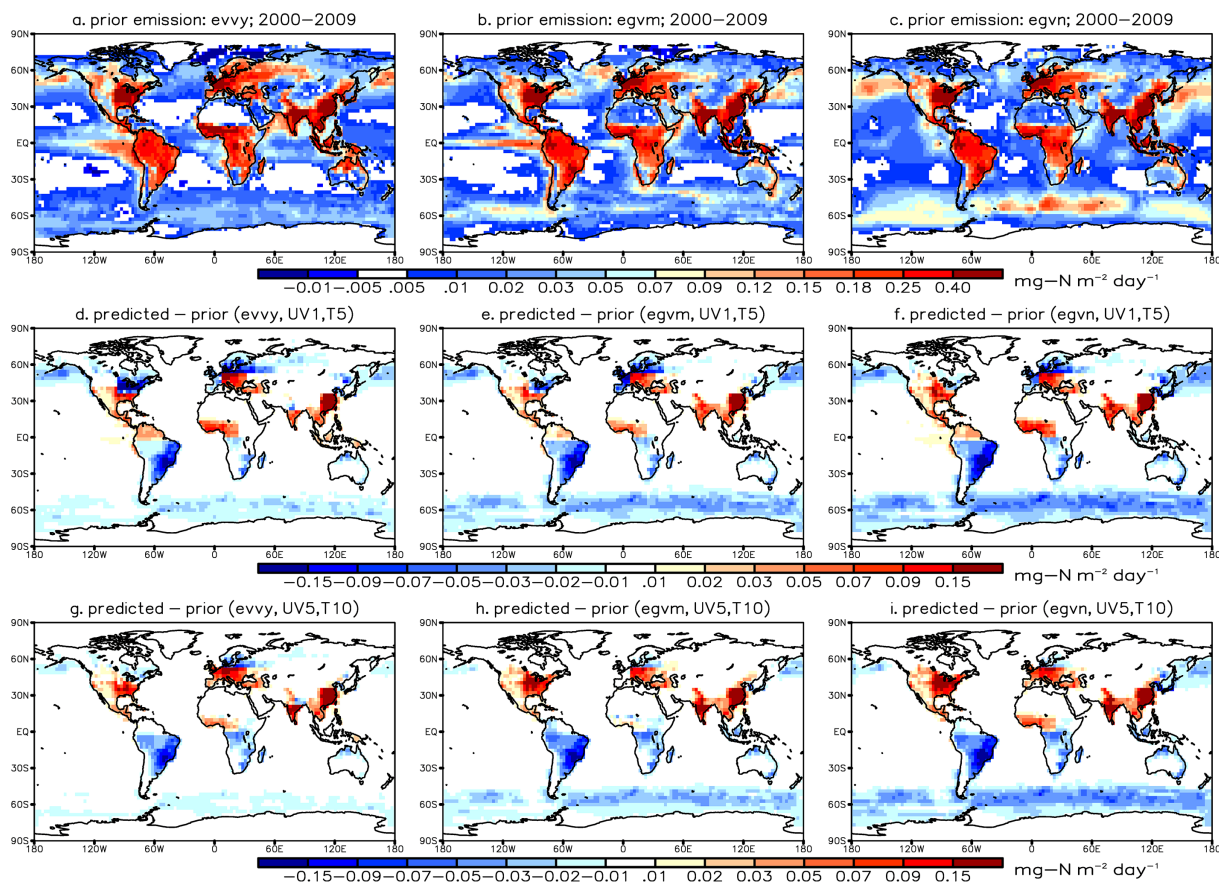
Fig. 7.   Maps of prior N$_2$O emission distributions (top row) and the predicted increments by the inversion relative to the prior fluxes (middle row: control transport, bottom row: weakly nudged transport).

sion cases. The predicted ocean emissions show the greatest corrections over the Southern Ocean region for the Nevison emission case (Fig. 7f) and the smallest for the Yang-scaled emission case (Fig. 7d). The inversions using WN forward runs show smaller flux corrections in the higher latitudes in both the hemispheres (Figs. 7g–i), compared with those using control transport (Figs. 7d–f). The land and ocean regions in the latitudes north of $\sim 40°N$ show smaller flux corrections (no deep-blue colors in Figs. 7g–i), which are compensated by an increase in emissions over the land south of $\sim 40°N$. Similarly, the flux corrections are milder over the Southern Ocean, as lighter blue colors are seen in Figs. 7g–i when compared with those in Figs. 7d–f.

3.2   Global total N$_2$O flux variability

Figure 8 shows the time evolution of global land and ocean emissions for each of the inversion en-

semble members with varying PFU for MDU_93 %. Expectedly, the interannual variability is greater for the inversions using greater PFUs, but the phase of the variations remained largely consistent between the inversions, particularly for the land. Significant downward corrections are found for the global ocean emissions by the inversions (except for the ACTM-egvyl case, which had lower emissions). The best estimate case (PFU_50 %) shows that the predicted mean ocean emission is lower by ~ 0.5 TgN yr^{-1} relative to the mean ocean prior (Fig. 8g), and the difference is as large as ~ 1.0 TgN yr^{-1} for the PFU_100 % case (Fig. 8h). This suggests that the N$_2$O emission distribution by Yang et al. (2020) and also the more severe scaling down to 2.67 TgN yr^{-1} is a better choice for the MIROC4-ACTM forward and inversion models, with lower emissions from the Southern Ocean region (Fig. 7).

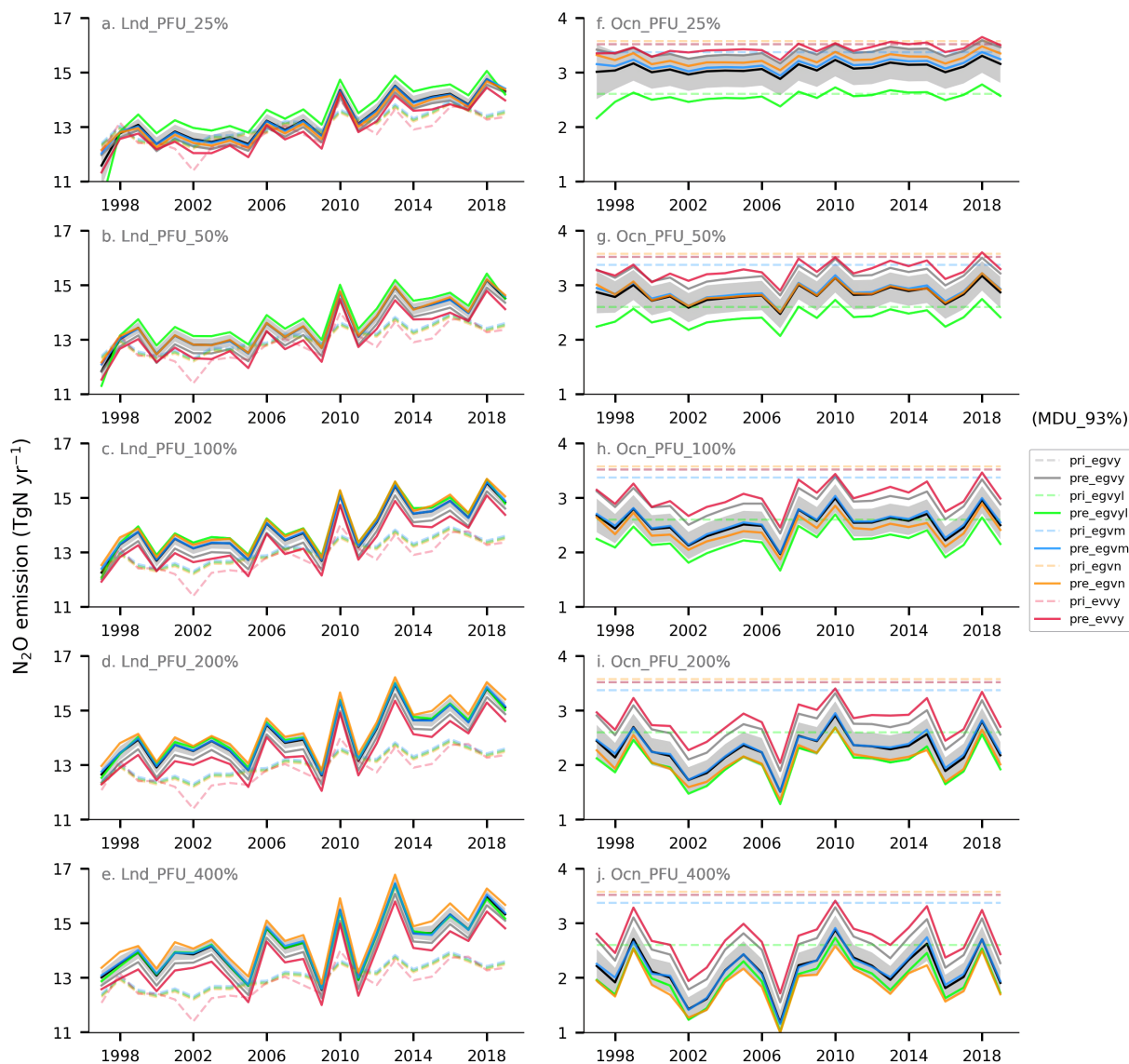Figure 9 shows the global land and ocean N$_2$O

Fig. 8.   Global land (a–e) and ocean (f–j) N$_2$O fluxes at annual time intervals (case: MDU_93 %, PFU = 25–400 %). The black lines and the shaded gray regions show mean and 1-σ standard deviations for the predicted emissions.

emission anomalies for the MDU_93 % case. The monthly anomalies are calculated by subtracting a long-term mean seasonal cycle from the monthly emissions for 1997–2019. Therefore, the time series contains both the interannual variability and long-term trends for the analysis period. The global land emissions increased by approximately ~ 1.7 TgN yr^{-1} between the first 5 years (1997–2001) and final 5 years (2015–2019) of the analysis (70 % greater than the prior estimate), whereas the global ocean shows marginal or no increase. We found a statistically

significant correlation between the predicted emission variability with the ENSO cycle for both global land and ocean ($p < 0.0002$). These flux variability, in phase for the ocean and land, explain part of the apparent increase in the growth rate during or following a La Niña, and the decrease during or following an El Niño phase (Fig. 4) (Ishijima et al. 2009; Thompson et al. 2014a). The anomalous wet conditions in the tropical land during the La Niña promote higher N$_2$O emissions under the anaerobic soil conditions with the availability of C and N substrates (e.g., Barrat
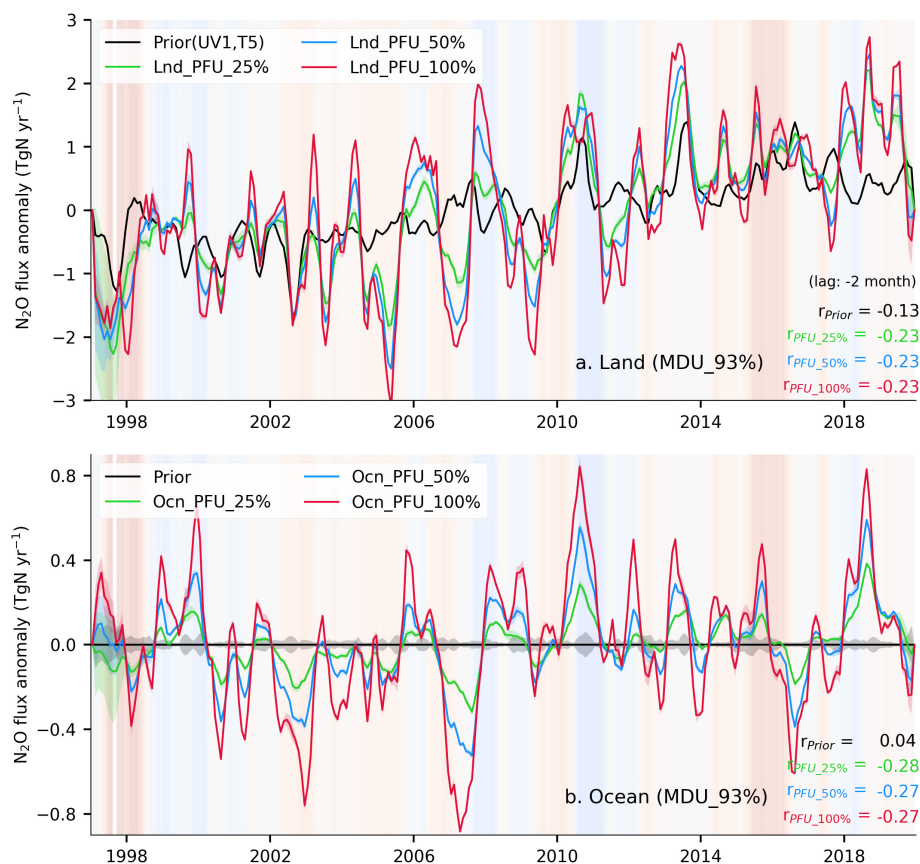
Fig. 9.   Global land (a) and ocean (b) flux anomalies are shown by taking 3-monthly moving window averages on the anomalies at monthly time intervals. Correlation coefficients (r) between the ENSO index (shaded) and the N_2O flux anomalies are given within each panel. Note that higher r-values are calculated when the land emissions lagged the ENSO index.

et al. 2021). Nevertheless, large uncertainties remain regarding the environmental controls on nitrification and denitrification pathways that produce N_2O in the soil, and the proportion of soil N_2O that could escape to the atmosphere (e.g., Wang et al. 2021). Note that the correlation of prior land emission anomalies, due to the VISIT agriculture and natural soil emissions (ref. Fig. 8), is less significant for the ENSO (maximum correlations lag/lead by approximately 6 months), suggesting that a better representation of the climate impact on the nitrogen cycle for both the seasonal and decadal timescales is needed in the terrestrial ecosystem models.

3.3   Regional N_2O fluxes from inverse modeling

Figures 10 and 11 respectively show the regional land and ocean emissions and their annual mean anomalies. Many of the land regions show large inter-annual variability and systematic increases in predicted emissions for 1997–2019 (colored lines), and the systematic increases are in phase with the prior emission scenarios for most regions (gray line). This suggests the VISIT model, driven by the fertilizer input data from FAOSTAT, reasonably well simulates the N_2O emissions from agricultural activities. The notable exceptions are Tropical America and Central Africa regions, where the rate of predicted emission increases are at least twice as fast as the prior emission increase rate (Figs. 10d, h). This supports the idea of underestimation of the N_2O emission factors per kilogram of fertilizer into the agricultural land in some parts of the world (Thompson et al. 2019). The interannual variability caused presumably by natural climate variations such as ENSO, are in weaker agreement between the prior and predicted emissions for most regions, but exceptionally good covariations seen
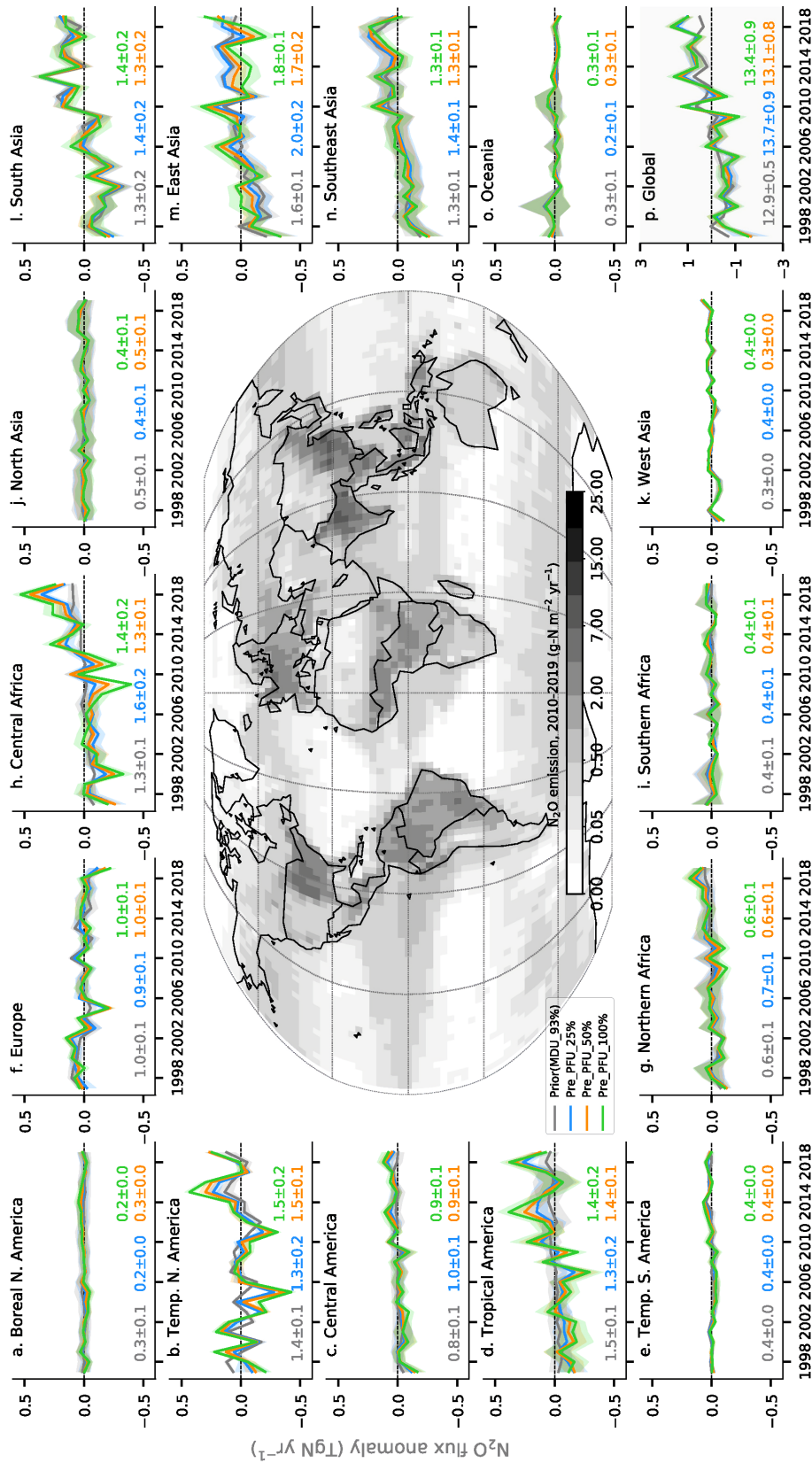
Fig. 10. Regional N$_2$O emissions for land regions, marked by the dark lines within the continents (case: MDU = 93 %, PFU = 25−100 %). The long-term (1997−2019) mean regional emission and 1-σ standard deviation are given within each panel, which are subtracted from the annual mean emission time series for calculation of the anomalies.
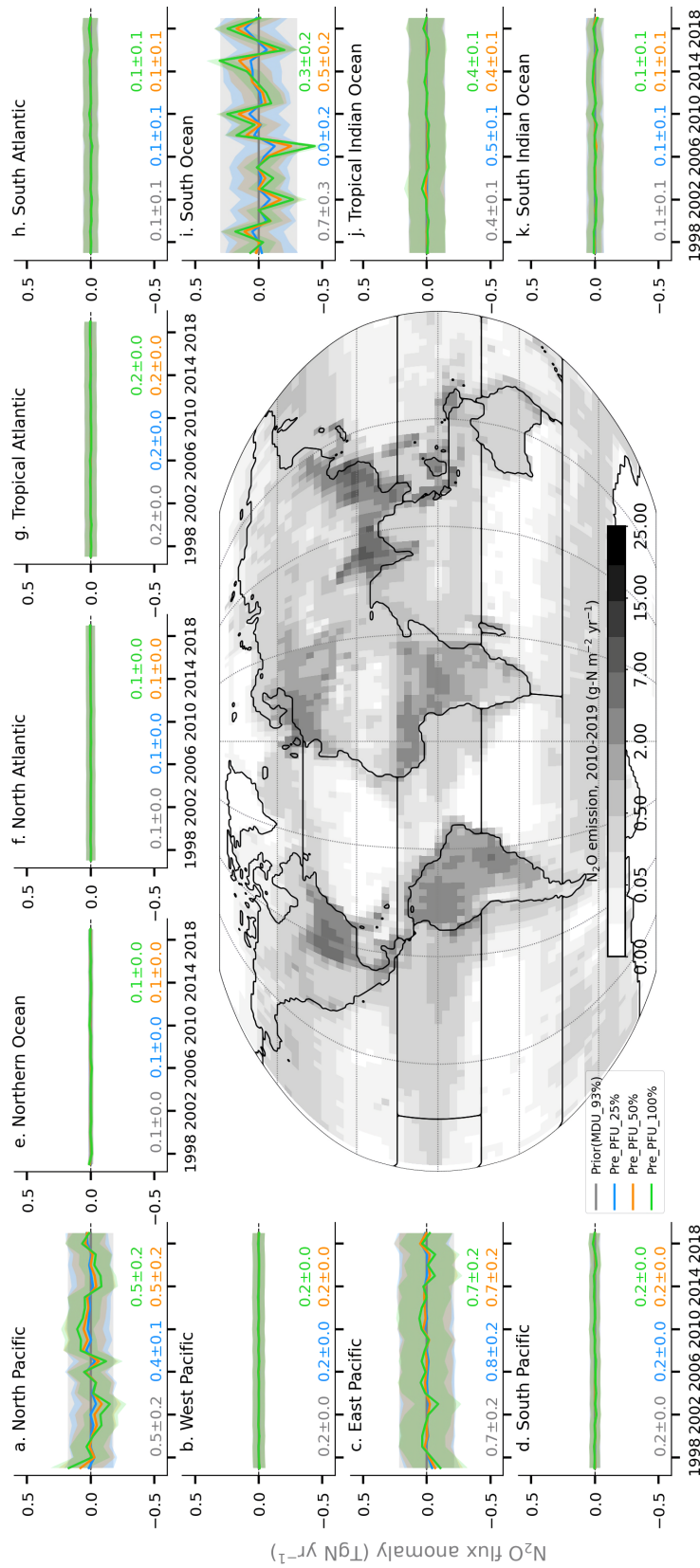
Fig. 11. Regional N_2O emissions for the ocean regions, marked by the dark lines (case: MDU = 93 %, PFU = 25–100 %). The long-term (1997–2019) mean regional emission and 1-σ standard deviation are given within each panel, which are subtracted from the annual mean emission time series for calculation of the anomalies.
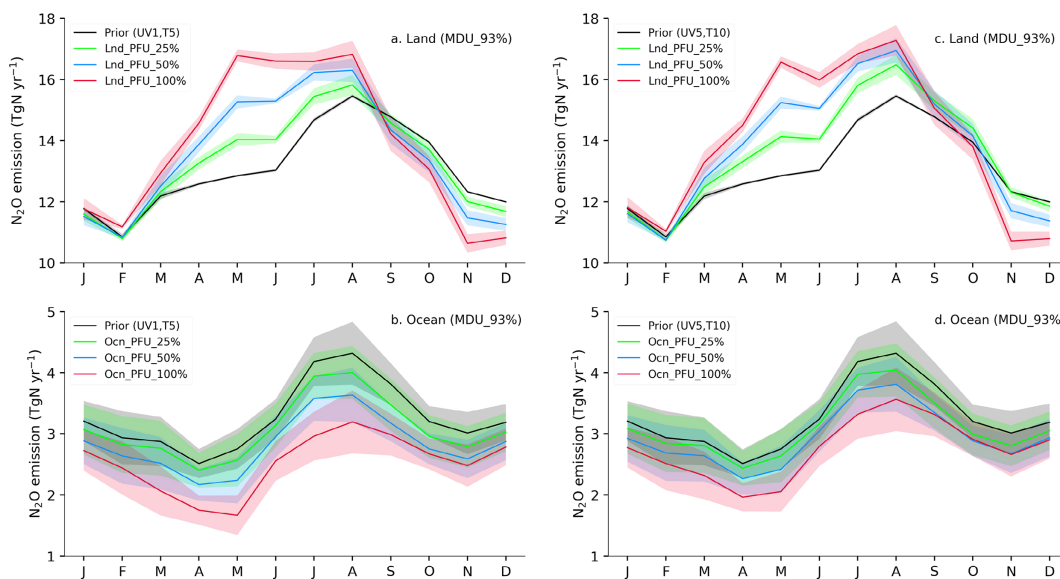
Fig. 12.   Seasonal cycles of total land and ocean fluxes are shown for two cases of MIROC4-ACTM simulations, control transport (a, b), and weakened nudging (c, d).

for the Temperate North America and South, East, and Southeast Asia regions (Figs. 10b, l–n). As discussed in detail earlier (Petrescu et al. 2021), our results confirm a reduction in N_2O emissions from Europe over the period of this analysis. This emission reduction is almost entirely caused by the adaptation of new technology in the chemical industry, which manufactured nitric acid for fertilizer production mainly and adipic acid for nylon production mainly (EDGAR_v5.0).

The ocean regions of the North Pacific, East Pacific, Southern Ocean, and Tropical India Ocean release approximately 60 % of the global ocean N_2O emissions. Interannual variations are small for most regions, except for the Southern Ocean and North and East Pacific. No cause for this interannual variability could be proposed here, whereas it is expected that N_2O ventilation through coastal ocean upwelling will drive the interannual variations in emissions. An expansion of the oxygen-deficient waters in the coastal ocean or increased ocean acidification due to anthropogenic activities would drive upward emission trends in global N_2O emissions (Breider et al. 2019; Naqvi et al. 2010). Detection of trends in regional N_2O emission by inverse modeling would be difficult given the uncertainties in ACTM simulations, measurement precision, and limited sampling network, because only a small increase is estimated for global total emissions, mostly below 0.3 TgN yr^{-1}, between the two decades of the 2000s and the 2010s (Table 3).

3.4 N_2O flux seasonal cycles

The seasonal cycles in global and regional emissions are important for understanding the drivers of the N_2O changes in the atmosphere. N_2O at the measurement sites varies because of changes in seasonal transport (vertical and horizontal including the effects of loss in the stratosphere) and surface emissions. For N_2O, vertical transport (stratosphere–troposphere exchange) is one of the major drivers, as the emissions of N_2O show relatively little variation at regional to global scales (Ishijima et al. 2010; Jiang et al. 2007; Nevison et al. 2007). However, at the locations of strong coastal upwelling, the N_2O seasonal cycle is observed to be influenced by sea–air fluxes due to winds and ΔpN_2O (Ganesan et al. 2020; Yang et al. 2020). Figure 12 shows mean (1997–2019) monthly variations in global land and ocean using the control and transport sensitivity simulations. Inversions using both forward simulations suggest that land emissions should increase by more than 4 TgN yr^{-1} relative to the prior emissions in the months of May and June. The land emissions are suggested to have a broad emission peak during May–August by the inversions at PFU_100 % instead of the sharper peak in August in the prior. The fundamental mode of a priori ocean emissions is not revised by the inversions (only systematic downward emission corrections are seen).

Figure 13 shows the mean seasonal variations over the 15 land and 11 ocean regions, which suggest
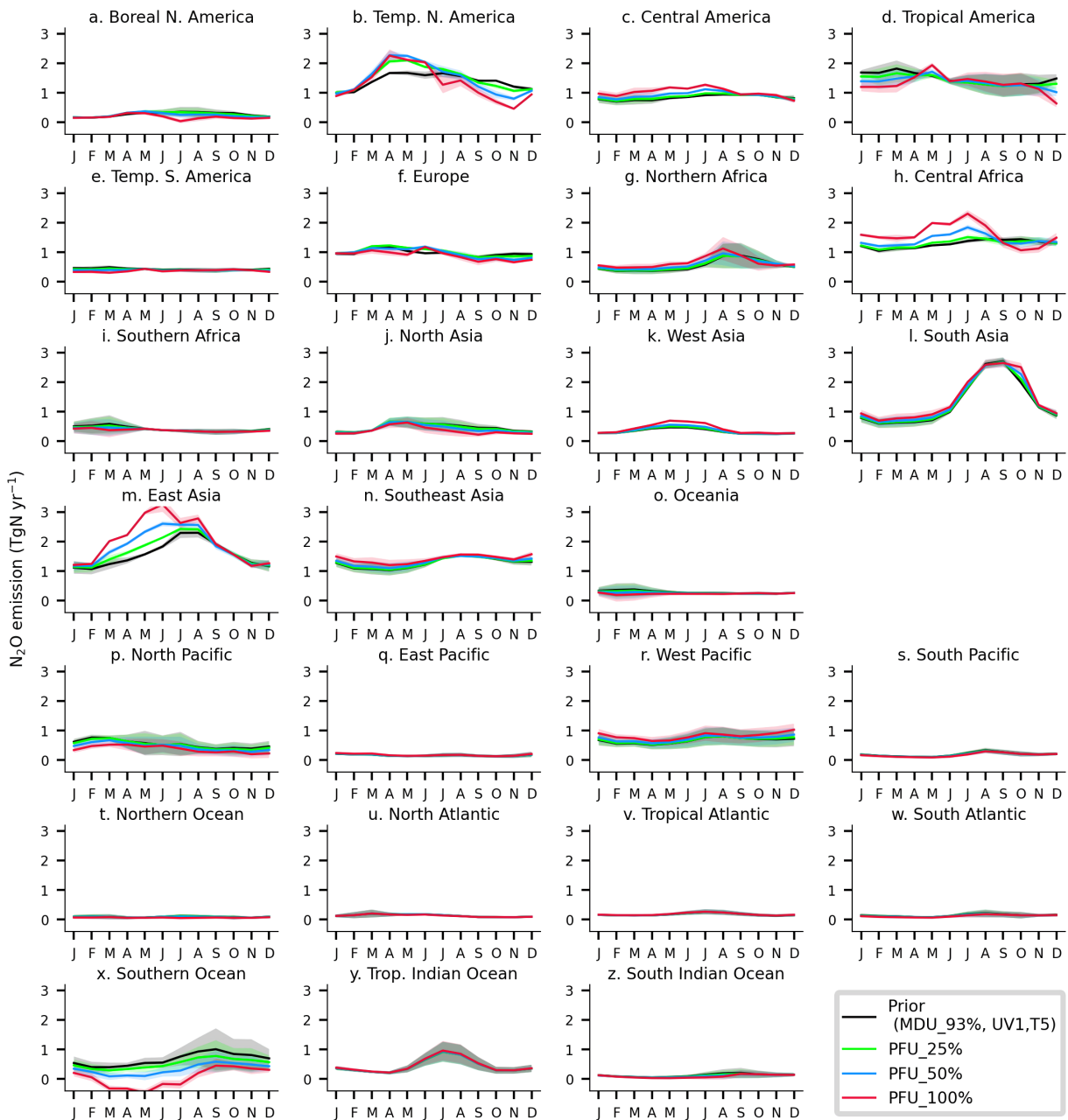
Fig. 13.   Regional N$_2$O fluxes for 15 land and 11 ocean regions (inversion cases for individual ensemble cases and weakly nudged transport are given in Fig. S4 and Fig. S5, respectively). The y-axis range is kept the same for all panels to highlight the regions of large emission increments by inversion.

that only Temperate North America, Central Africa, and East Asia (panels b, h, and m, respectively) are the regions where an early peak in N$_2$O emissions is estimated by the inversions, compared with the prior emission model. The seasonality predicted by our inversions is in good agreement with the regional

study for North America that estimated maximum emissions in spring/early summer, consistent with a nitrogen fertilizer-driven source (Nevison et al. 2018). Additionally, Fig. 7f suggests that emissions over the mid-west USA should be higher in the case of ACTM-evvy. A closer look at the individual ensemble emis-
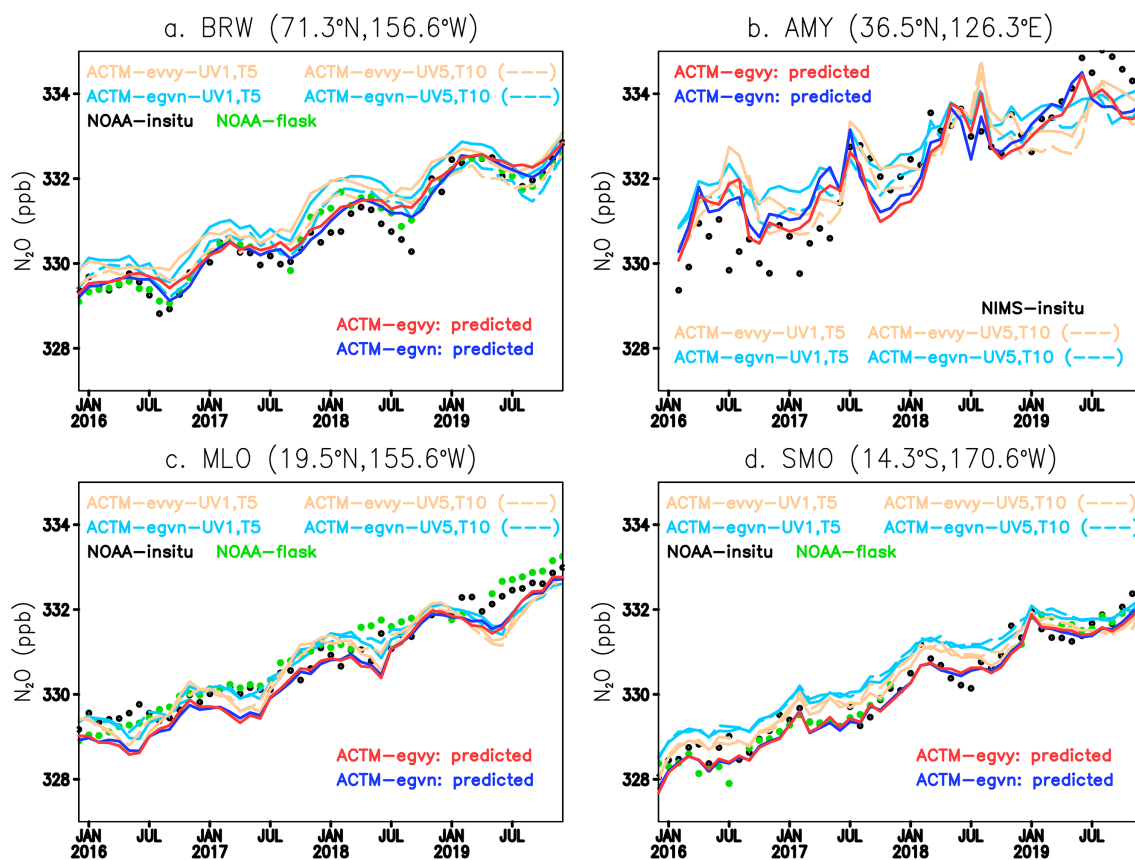
Fig. 14. Examples of the observed and model N_2O time series at BRW, AMY, MLO, and SMO. The prior model simulations (light blue and orange lines, solid and broken lines are for cases evvy and egvn, respectively) are added/subtracted arbitrary offsets for fitting the results on the common y-axis for comparison. Model simulations for different heights and more emission ensemble cases are compared with the measurements at MLO in Fig. S3.

sion cases (Fig. S4) suggests that the inverse model is not able to constrain the seasonal emissions for most regions (where the phase of inverted seasonal cycles remained close to the priors) because of the lack of measurements within the regions or in the downwind regions. Because the two sites in Japan (HAT and COI) are located downwind of continental East Asia, we find that all inversions agree on a common seasonal cycle, despite the differences between the prior emission seasonality (Fig. S4m). Similar good agreements in the predicted emission seasonality are found for Temperate in North America, Europe, and to some extent, Boreal North America (Figs. S4b, f, a, respectively).

3.5 Atmospheric N_2O seasonal cycle

We compare the N_2O simulations using two emission cases (egvn and evvy) with observations at four selected sites (Fig. 14). These sites are chosen because of their unique characteristics and the challenges they pose for the chemistry-transport models (e.g., Thompson et al. 2014a). We also test the model simulations using the control transport and weak nudging cases (shown by solid and broken lines, respectively). Generally, the weak nudging case shows a slower rate of N_2O increase when compared with the control transport case for a given emission, arising because of faster upward transport of N_2O into the stratosphere (Figs. S1, S2), and resulting shorter lifetime. Of particular interest here are differences in seasonal N_2O variations; the comparisons suggest the N_2O seasonal cycles in ACTM-egvn (light blue lines) are apparently in a better match with a relatively weak seasonal variability as measured at MLO (Fig. 14c), which was deeper for ACTM-evvy case (brown lines). The seasonal cycle simulations for the two transport cases

do not show observable differences at all four sites in most years (Figs. 14a, b, d; solid vs broken lines). The simulations for three sites, except for SMO, show clear differences between the choice of emissions (Fig. 14a; orange vs light blue lines), which are revised by inverse modeling to produce consistent phase and amplitude (red/blue lines). However, for MLO, the seasonal cycle phase and amplitude did not produce an improved agreement with observations, indicating that a systematic transport bias rather than emissions cause the model error. The agreement between the simulated and observed N_2O matches well at AMY, Korea after inversion, where the regional emissions are constrained by the site at HAT, Japan. AMY site samples airmass of local emission activities related to agriculture, such as rice paddies, sweet potatoes, and onions, and long-range transport from mainland China (Lee et al. 2020).

Nevertheless, the inversions did not improve the model–observation comparison of the N_2O seasonal cycle at MLO (Fig. 14c). To disentangle the role of chemistry (through the stratosphere–troposphere exchange) or transport in the troposphere, we have conducted SF_6 simulations (Fig. 15). The SF_6 simulation using weaker nudging (case UV5,T10) does not support better stratosphere–troposphere exchange in MIROC4-ACTM compared with that used as our control simulation (UV1,T5), particularly at MLO. It is thus, a possibility that the photochemical loss processes involving solar UV radiation [and $O(^1D)$] are poorly modeled in ACTM, e.g., a stronger N_2O sink in the lower stratosphere would bring N_2O-depleted air to the troposphere at the latitudes of the stratospheric "surf-zone", which moves with the location of the subtropical jet streams (Bisht et al. 2021). Bisht et al. (2021) showed (their Fig. 2) that the MIROC4-ACTM-simulated N_2O vertical profile gradient in the lower stratosphere is greater or comparable with the observed in most seasons, whereas the vertical gradients for SF_6, CO_2, and CH_4 are weaker in the model than those observed. This implied that faster troposphere–stratosphere transport is compensated by a stronger sink in the lower stratosphere for N_2O (the other three species have weaker or no photochemical loss). Because stratosphere–troposphere exchange is an upper tropospheric process, that effect is not corrected by the inversions using the measurements mainly at the surface. However, an overall increase in N_2O emission would be predicted by the inversions in the tropical latitudes (Fig. 7), which could be evaluated using global observations.
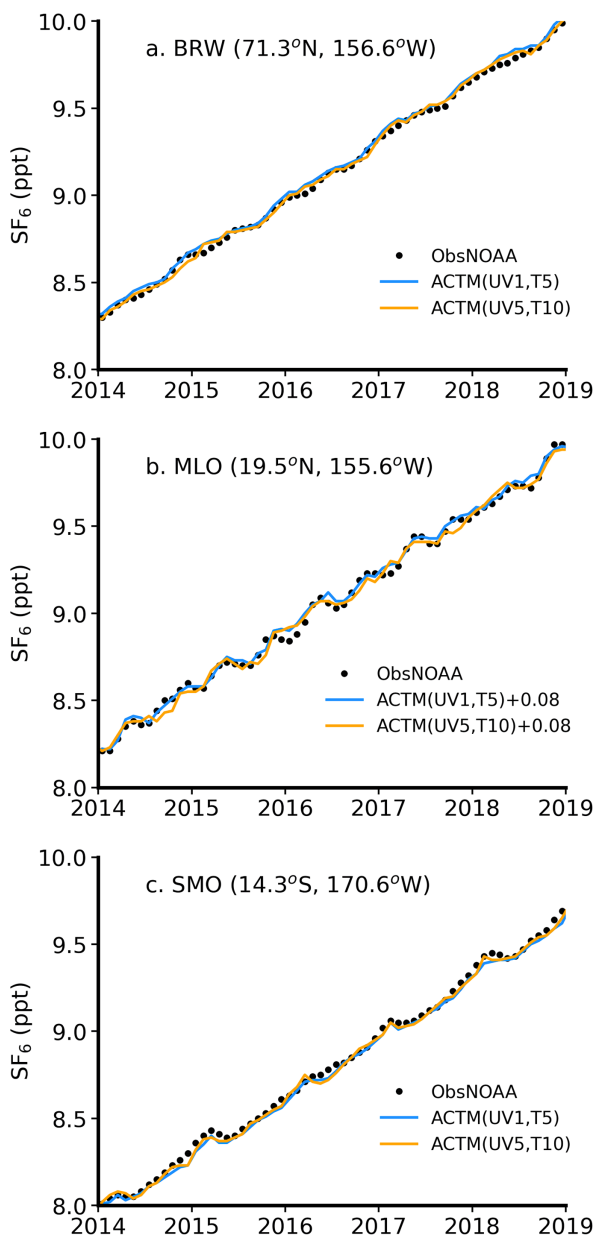

Fig. 15. Time series of SF_6 observed at NOAA flask-air sampling sites Barrow (BRW), Mauna Loa (MLO), and Samoa (SMO), in comparison with those simulated by the two transport simulations by MIROC4-ACTM.

3.6 Evaluation of modeled N_2O mixing ratios using aircraft observations

Finally, we briefly evaluate the inversions using independent aircraft campaigns, limited to the HIAPER Pole-to-Pole Observations (HIPPO) (Kort et al. 2011;

Wofsy 2011). Table S2 shows that there is a systematic bias, with observations being systematically higher than the inversion results. This is due to the known offsets between the quantum cascade laser spectrometer (QCLS) and NOAA flask measurement onboard the HIPPO campaigns although the HIPPO QCLS measurements are calibrated against the NOAA 2006 scale (Santoni et al. 2014). Santoni et al. (in their Table 4, Fig. 12) calculated NOAA–QCLS biases of −0.61, −1.18, −1.15, −1.23, and −1.18 ppb for HIPPO 1−5 campaigns, respectively, and these biases are in good agreement with the mean ACTM–QCLS biases for all inversions (−0.99, −1.58, −1.23, −1.20, and −1.19 ppb, respectively; ref. Table S2). The inversion results also successfully predicted known scale differences between NOAA and AGAGE or NIES observations (by two inversions with and without scale adjustments to the NOAA and AGAGE data; Section 2.3).

The tropical bulge in N_2O observed during the 1st HIPPO campaign (Kort et al. 2011) and some of the latter HIPPO campaigns is still not produced by any of the MIROC4-ACTM simulations and the subsequent inversions (Fig. S6). This could be due to the greater influx of N_2O-depleted air through stratosphere–troposphere exchange as discussed earlier. For all other HIPPO campaigns, the model–observation comparisons produced meridional gradients satisfactorily, within the variabilities for any given 10−20° latitude bands. The finer-scale meridional variability could be obscured due to the coarse model horizontal resolution of approximately 2.8° × 2.8°.

The Northern to Southern Hemisphere (NH-SH) N_2O gradients are better simulated by the MIROC4-ACTM control transport simulations (both prior and predicted emission cases), compared with the weakly nudged transport case that underestimates the gradients by 19−63 % relative to the control case (Fig. 16). Between the five ensemble emission cases, the prior simulation using Nevison et al. (1995) ocean flux produced the smallest NH-SH gradient in all the seasons covered by the [HIPPO campaigns, intermediate values using Manizza et al. (2012), and greatest for Yang et al. (2020) emission case, which are expected from their emission distributions (Figs. 7a−c)]. The simulations using predicted fluxes produced rather similar NH-SH gradients for all the emission ensemble members and PFU sensitivity cases, but the mean gradients are found to be greater by 0.1−85 % relative to a priori case. For three out of five HIPPO campaigns, the predicted model produced better or similar agreement as that for the a priori model. The meridional
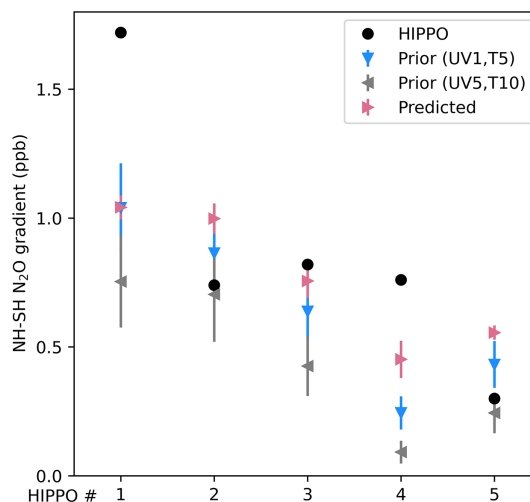

Fig. 16. Northern to Southern (NH-SH) gradients in N_2O as observed by the five HIPPO campaigns and simulated by ACTM for a priori emissions (two cases) and predicted emissions. Plots show mean and 1-σ standard deviations over the five emission cases (ref. Table S2). Data below 3 km are used for calculation, and the NH and SH are divided at the equator.

profile during HIPPO-5 is not simulated well by all models in the altitude range of 1−3 km but very well simulated in 4−7 km (Figs. S6k, l). The 1-σ standard deviations of the model–observation differences do not provide any information on the quality of the prior fluxes or the transport sensitivity simulations (Table S2). The differences decrease for the predicted emission simulations when compared with the prior emission simulations.

4. Conclusions

We have conducted forward transport modeling of atmospheric N_2O (1971−2020) using MIROC4-ACTM and inverse modeling to estimate N_2O emissions over the globe using the measurements of NOAA, AGAGE, and NIES at 42 sites and MIROC4-ACTM simulations. First, the MIROC4-ACTM simulations are compared with the long-term (1978−2019) records of N_2O at a few sites of AGAGE and NOAA, which led us to conclude that global N_2O emissions from ocean and land surfaces are fairly well developed in recent years for simulating the atmospheric burden of N_2O. The lifetime of N_2O in the MIROC4-ACTM control transport simulation is estimated to be 127.6 ± 4.0 yr for 1990−2019, but it has a sensitivity to the model transport. Our "control" simulations are nudged

to Japanese 55-year reanalysis products of U, V, and T with Newtonian relaxation times of 1, 1, and 5 days, respectively, and a transport sensitivity simulation used relaxation times of 5, 5, and 10 days.

More than 100 inversions were performed to analyze the role of prior flux estimates/uncertainties and measurement data uncertainty models as input to the inversion model. Using the χ^2-test of corrections to the prior fluxes and fitting to the observations, both weighed by their uncertainties, we have selected the preferred inversion. By inverse modeling, we aimed mainly at revisions of global land–ocean partitioning of emissions as well as regional emission estimates at subcontinental scales. The prior land emissions of 12.58 ± 0.35 TgN yr^{-1} and 13.41 ± 0.28 TgN yr^{-1}, respectively, for the 2000s and 2010s, are revised to 12.99 ± 0.22 TgN yr^{-1} and 14.30 ± 0.20 TgN yr^{-1}, and the prior ocean emissions of 3.40 ± 0.41 TgN yr^{-1} are revised to 2.74 ± 0.27 TgN yr^{-1} and 2.91 ± 0.27 TgN yr^{-1}, respectively, for the 2000s and 2010s using the preferred inversion. The majority of the reductions in the ocean emissions occurred over the Southern Ocean region, and the land emissions increased predominantly over the northern tropics and extra-tropics.

We find that N$_2$O shows higher growth rates during the La Niña years or in the following months, compared with those during the El Niño years. An analysis of the monthly mean emission variabilities shows statistically significant correlations with the ENSO cycle (maximum correlation at a lag-time of 2 months for the land); high emissions during and after La Niña years and vice versa for the El Niño years. These variabilities originated in the tropical land regions. At regional scales, we also find a large increase of N$_2$O emissions over Temperate North America; Central and Tropical America; Northern and Central Africa; and South, East, and Southeast Asia during the 1997–2019 period.

On seasonal time scales, a large modification and a broader peak in global land emissions during May–August is predicted compared with the land prior emission seasonality in the inversions. The land seasonal cycles are revised over Temperate North America, Central Africa, and East Asia. These corrections to the N$_2$O emission seasonal cycles are fairly independent of MIROC4-ACTM transport uncertainties. An earlier peak in the Temperate North America emissions could be confirmed by the timing of fertilizer application on agricultural land and thawing of frozen soil (an earlier peak is also estimated for East Asia but no independent study for a comparison). This information would be of potential interest for refining terrestrial ecosystem models of nitrogen cycling, such as VISIT, which was used as the prior in our study.

The validation of ACTM transport for two different nudging strengths remained ambiguous using SF$_6$ time series at surface sites or high-altitude balloon observations of N$_2$O for improved simulation of the seasonal cycle at Mauna Loa, whereas the simulations using a priori emissions clearly produced a better agreement with the observed seasonal cycle at other two remote sites (Barrow, Samoa). Finally, the evaluation of inversion results using independent measurements of N$_2$O, e.g., the HIPPO campaigns, suggests minor improvements for the NH-SH gradients and 1-σ standard deviations by the inversions relative to those using prior emissions. A systematic bias of approximately 1 ppb is estimated for the HIPPO observations compared with the NOAA/WMO calibration scale. Further development for critical validation of the inversion emissions is required.

Supplements

The supplemental document provides a brief history of the evolution in N$_2$O measurement systems (the 1970s to present), Supplementary Table S1, and Supplementary Figs. S1–S6.

The datasets generated and/or analyzed during the current study are available in the JAMSTEC repository, https://doi.org/10.5281/zenodo.5875385.

The datasets used and/or analyzed during the current study are also available from the corresponding author on reasonable request.

All data generated or analyzed during this study are included in this published article (and its supplementary information files). AGAGE data are available at https://agage.mit.edu/data. NOAA data are available at https://gml.noaa.gov/hats/combined/N2O.html and https://gml.noaa.gov/ccgg/flask.html. NIES data are available at https://db.cger.nies.go.jp/portal/geds/atmosphericAndOceanicMonitoring, and NIMS data are available at the WDCGG (https://gaw.kishou.go.jp).

References

Barrat, H. A., J. Evans, D. R. Chadwick, I. M. Clark, K. Le Cocq, and L. M. Cardenas, 2021: The impact of drought and rewetting on N_2O emissions from soil in temperate and Mediterranean climates. *Eur. J. Soil Sci.*, **72**, 2504–2516.

Bisht, J. S. H., T. Machida, N. Chandra, K. Tsuboi, P. K. Patra, T. Umezawa, Y. Niwa, Y. Sawa, S. Morimoto, T. Nakazawa, N. Saitoh, and M. Takigawa, 2021: Seasonal variations of SF_6, CO_2, CH_4, and N_2O in the UT/LS region due to emissions, transport, and chemistry. *J. Geophys. Res.: Atmos.*, **126**, e2020JD033541, doi: 10.1029/2020JD033541.

Bouwman, A. F., A. H. W. Beusen, J. Griffioen, J. W. Van Groenigen, M. M. Hefting, O. Oenema, P. J. T. M. Van Puijenbroek, S. Seitzinger, C. P. Slomp, and E. Stehfest, 2013: Global trends and uncertainties in terrestrial denitrification and N_2O emissions. *Philos.*

Trans. Roy. Soc. London, Ser. B, **368**, 20130112, doi: 10.1098/rstb.2013.0112.

Breider, F., C. Yoshikawa, A. Makabe, S. Toyoda, M. Wakita, Y. Matsui, S. Kawagucci, T. Fujiki, N. Harada, and N. Yoshida, 2019: Response of N_2O production rate to ocean acidification in the western North Pacific. *Nat. Climate Change*, **9**, 954–958.

Buitenhuis, E. T., P. Suntharalingam, and C. Le Quéré, 2018: Constraints on global oceanic emissions of N_2O from observations and models. *Biogeosciences*, **15**, 2161–2175.

Butterbach-Bahl, K., E. M. Baggs, M. Dannenmann, R. Kiese, and S. Zechmeister-Boltenstern, 2013: Nitrous oxide emissions from soils: How well do we understand the processes and their controls? *Philos. Trans. Roy. Soc. London, Ser. B*, **368**, 20130122, doi:10.1098/rstb.2013.0122.

Crippa, M., E. Solazzo, G. Huang, D. Guizzardi, E. Koffi, M. Muntean, C. Schieberle, R. Friedrich, and G. Janssens-Maenhout, 2020: High resolution temporal profiles in the Emissions Database for Global Atmospheric Research. *Sci. Data*, **7**, 121, doi:10.1038/s41597-020-0462-2.

Crutzen, P. J., and D. H. Ehhalt, 1977: Effects of nitrogen fertilizers and combustion on the stratospheric ozone layer. *Ambio*, **6**, 112–117.

Dlugokencky, E. J., L. P. Steele, P. M. Lang, and K. A. Masarie, 1994: The growth rate and distribution of atmospheric methane. *J. Geophys. Res.*, **99**, 17021–17043.

Dutkiewicz, S., M. J. Follows, and P. Parekh, 2005: Interactions of the iron and phosphorus cycles: A three-dimensional model study. *Global Biogeochem. Cycles*, **19**, GB1021, doi:10.1029/2004GB002342.

Eggleston, S., L. Buendia, K. Miwa, T. Ngara, and K. Tanabe, 2006: *2006 IPCC Guidelines for National Greenhouse Gas Inventories*. [Available at https://www.ipcc-nggip.iges.or.jp.]

Etminan, M., G. Myhre, E. J. Highwood, and K. P. Shine, 2016: Radiative forcing of carbon dioxide, methane, and nitrous oxide: A significant revision of the methane radiative forcing. *Geophys. Res. Lett.*, **43**, 12614–12623.

Fahey, D. W., P. A. Newman, J. A. Pyle, B. Safari, M. P. Chipperfield, D. J. Karoly, D. Kinnison, M. K. Ko, and M. Santee, 2018: *Scientific Assessment of Ozone Depletion: 2018*. Global Ozone Research and Monitoring Project–Report No. 58, World Meteorological Organization, Geneva, Switzerland, 590 pp.

Ganesan, A. L., M. Manizza, E. J. Morgan, C. M. Harth, E. Kozlova, T. Lueker, A. J. Manning, M. F. Lunt, J. Mühle, J. V. Lavric, M. Heimann, R. F. Weiss, and M. Rigby, 2020: Marine nitrous oxide emissions from three Eastern Boundary Upwelling Systems inferred from atmospheric observations. *Geophys. Res. Lett.*, **47**, e2020GL087822, doi:10.1029/2020GL087822.

Hall, B. D., G. S. Dutton, and J. W. Elkins, 2007: The NOAA nitrous oxide standard scale for atmospheric observations. *J. Geophys. Res.*, **112**, D09305, doi: 10.1029/2006JD007954.

Hirsch, A. I., A. M. Michalak, L. M. Bruhwiler, W. Peters, E. J. Dlugokencky, and P. P. Tans, 2006: Inverse modeling estimates of the global nitrous oxide surface flux from 1998–2001. *Global Biogeochem. Cycles*, **20**, GB1008, doi:10.1029/2004GB002443.

Huang, J., A. Golombek, R. Prinn, R. Weiss, P. Fraser, P. Simmonds, E. J. Dlugokencky, B. Hall, J. Elkins, P. Steele, R. Langenfelds, P. Krummel, G. Dutton, and L. Porter, 2008: Estimation of regional emissions of nitrous oxide from 1997 to 2005 using multinetwork measurements, a chemical transport model, and an inverse method. *J. Geophys. Res.*, **113**, D17313, doi: 10.1029/2007JD009381.

IPCC, 2013: *Climate Change 2013: The Physical Science Basis. Contribution of Working Group I to the Fifth Assessment Report of the Intergovernmental Panel on Climate Change.* Stocker, T. F., D. Qin, G.-K. Plattner, M. Tignor, S. K. Allen, J. Boschung, A. Nauels, Y. Xia, V. Bex, and P. M. Midgley (eds.), Cambridge University Press, 1535 pp.

Ishijima, K., S. Sugawara, K. Kawamura, G. Hashida, S. Morimoto, S. Murayama, S. Aoki, and T. Nakazawa, 2007: Temporal variations of the atmospheric nitrous oxide concentration and its δ^{15}N and δ^{18}O for the latter half of the 20th century reconstructed from firn air analyses. *J. Geophys. Res.*, **112**, D03305, doi:10.1029/ 2006JD007208.

Ishijima, K., T. Nakazawa, and S. Aoki, 2009: Variations of atmospheric nitrous oxide concentration in the northern and western Pacific. *Tellus B*, **61**, 408–415.

Ishijima, K., P. K. Patra, M. Takigawa, T. Machida, H. Matsueda, Y. Sawa, L. P. Steele, P. B. Krummel, R. L. Langenfelds, S. Aoki, and T. Nakazawa, 2010: Stratospheric influence on the seasonal cycle of nitrous oxide in the troposphere as deduced from aircraft observations and model simulations. *J. Geophys. Res.*, **115**, D20308, doi:10.1029/2009JD013322.

Ito, A., 2019: Disequilibrium of terrestrial ecosystem CO_2 budget caused by disturbance-induced emissions and non-CO_2 carbon export flows: A global model assessment. *Earth Syst. Dyn.*, **10**, 685–709.

Ito, A., K. Nishina, K. Ishijima, S. Hashimoto, and M. Inatomi, 2018: Emissions of nitrous oxide (N_2O) from soil surfaces and their historical changes in East Asia: A model-based assessment. *Prog. Earth Planet. Sci.*, **5**, 55, doi:10.1186/s40645-018-0215-4.

Jiang, X., W. L. Ku, R.-L. Shia, Q. Li, J. W. Elkins, R. G. Prinn, and Y. L. Yung, 2007: Seasonal cycle of N_2O: Analysis of data. *Global Biogeochem. Cycles*, **21**, GB1006, doi:10.1029/2006GB002691.

Ko, M. K. W., P. A. Newman, S. Reimann, and S. E. Strahan, 2013: *Lifetimes of stratospheric ozone-depleting*

substances, *their replacements, and related species*. SPARC Report No. 6, WCRP-15/2013, 255 pp.

Kort, E. A., P. K. Patra, K. Ishijima, B. C. Daube, R. Jiménez, J. Elkins, D. Hurst, F. L. Moore, C. Sweeney, and S. C. Wofsy, 2011: Tropospheric distribution and variability of N_2O: Evidence for strong tropical emissions. *Geophys. Res. Lett.*, **38**, L15806, doi:10.1029/2011GL 047612.

Lee, H., S.-O. Han, S.-B. Ryoo, J.-S. Lee, and G.-W. Lee, 2019: The measurement of atmospheric CO_2 at KMA GAW regional stations, its characteristics, and comparisons with other East Asian sites. *Atmos. Chem. Phys.*, **19**, 2149–2163.

Lee, H., E. J. Dlugokencky, J. C. Turnbull, S. Lee, S. J. Lehman, J. B. Miller, G. Pétron, J.-S. Lim, G.-W. Lee, S.-S. Lee, and Y.-S. Park, 2020: Observations of atmospheric $^{14}CO_2$ at Anmyeondo GAW station, South Korea: Implications for fossil fuel CO_2 and emission ratios. *Atmos. Chem. Phys.*, **20**, 12033–12045.

MacFarling Meure, C., D. Etheridge, C. Trudinger, P. Steele, R. Langenfelds, T. van Ommen, A. Smith, and J. Elkins, 2006: Law Dome CO_2, CH_4 and N_2O ice core records extended to 2000 years BP. *Geophys. Res. Lett.*, **33**, L14810, doi:10.1029/2006GL026152.

Manizza, M., R. F. Keeling, and C. D. Nevison, 2012: On the processes controlling the seasonal cycles of the air–sea fluxes of O_2 and N_2O: A modelling study. *Tellus B*, **64**, 18429, doi:10.3402/tellusb.v64i0.18429.

Nakazawa, T., M. Ishizawa, K. Higuchi, and N. B. A. Trivett, 1997: Two curve fitting methods applied to CO_2 flask data. *Environmetrics*, **8**, 197–218.

Naqvi, S. W. A., H. W. Bange, L. Farías, P. M. S. Monteiro, M. I. Scranton, and J. Zhang, 2010: Marine hypoxia/ anoxia as a source of CH_4 and N_2O. *Biogeosciences*, **7**, 2159–2190.

Nevison, C. D., R. F. Weiss, and D. J. Erickson III, 1995: Global oceanic emissions of nitrous oxide. *J. Geophys. Res.: Oceans*, **100**, 15809–15820.

Nevison, C. D., N. M. Mahowald, R. F. Weiss, and R. G. Prinn, 2007: Interannual and seasonal variability in atmospheric N_2O. *Global Biogeochem. Cycles*, **21**, GB3017, doi:10.1029/2006GB002755.

Nevison, C., A. Andrews, K. Thoning, E. Dlugokencky, C. Sweeney, S. Miller, E. Saikawa, J. Benmergui, M. Fischer, M. Mountain, and T. Nehrkorn, 2018: Nitrous oxide emissions estimated with the CarbonTracker-Lagrange North American regional inversion framework. *Global Biogeochem. Cycles*, **32**, 463–485.

Oreggioni, G. D., F. M. Ferraio, M. Crippa, M. Muntean, E. Schaaf, D. Guizzardi, E. Solazzo, M. Duerr, M. Perry, and E. Vignati, 2021: Climate change in a changing world: Socio-economic and technological transitions, regulatory frameworks and trends on global greenhouse gas emissions from EDGAR v.5.0. *Global Environ. Change*, **70**, 102350, doi:10.1016/j.gloenvcha. 2021.102350.

Parton, W. J., A. R. Mosier, D. S. Ojima, D. W. Valentine, D. S. Schimel, K. Weier, and A. E. Kulmala, 1996: Generalized model for N_2 and N_2O production from nitrification and denitrification. *Global Biogeochem. Cycles*, **10**, 401–412.

Patra, P. K., M. Takigawa, S. Watanabe, N. Chandra, K. Ishijima, and Y. Yamashita, 2018: Improved chemical tracer simulation by MIROC4.0-based atmospheric chemistry-transport model (MIROC4-ACTM). *SOLA*, **14**, 91–96.

Petrescu, A. M. R., C. Qiu, P. Ciais, R. L. Thompson, P. Peylin, M. J. McGrath, E. Solazzo, G. Janssens-Maenhout, F. N. Tubiello, P. Bergamaschi, D. Brunner, G. P. Peters, L. Höglund-Isaksson, P. Regnier, R. Lauerwald, D. Bastviken, A. Tsuruta, W. Winiwarter, P. K. Patra, M. Kuhnert, G. D. Oreggioni, M. Crippa, M. Saunois, L. Perugini, T. Markkanen, T. Aalto, C. D. G. Zwaaftink, H. Tian, Y. Yao, C. Wilson, G. Conchedda, D. Günther, A. Leip, P. Smith, J.-P. Haussaire, A. Leppänen, A. J. Manning, J. McNorton, P. Brockmann, and A. J. Dolman, 2021: The consolidated European synthesis of CH_4 and N_2O emissions for the European Union and United Kingdom: 1990–2017. *Earth Syst. Sci. Data*, **13**, 2307–2362.

Prather, M. J., J. Hsu, N. M. DeLuca, C. H. Jackman, L. D. Oman, A. R. Douglass, E. L. Fleming, S. E. Strahan, S. D. Steenrod, O. A. Søvde, I. S. A. Isaksen, L. Froidevaux, and B. Funke, 2015: Measuring and modeling the lifetime of nitrous oxide including its variability. *J. Geophys. Res.: Atmos.*, **120**, 5693–5705.

Prinn, R. G., R. F. Weiss, J. Arduini, T. Arnold, H. L. DeWitt, P. J. Fraser, A. L. Ganesan, J. Gasore, C. M. Harth, O. Hermansen, J. Kim, P. B. Krummel, S. Li, Z. M. Loh, C. R. Lunder, M. Maione, A. J. Manning, B. R. Miller, B. Mitrevski, J. Mühle, S. O'Doherty, S. Park, S. Reimann, M. Rigby, T. Saito, P. K. Salameh, R. Schmidt, P. G. Simmonds, L. P. Steele, M. K. Vollmer, R. H. Wang, B. Yao, Y. Yokouchi, D. Young, and L. Zhou, 2018: History of chemically and radiatively important atmospheric gases from the Advanced Global Atmospheric Gases Experiment (AGAGE). *Earth Syst. Sci. Data*, **10**, 985–1018.

Ravishankara, A. R., J. S. Daniel, and R. W. Portmann, 2009: Nitrous oxide (N_2O): The dominant ozone-depleting substance emitted in the 21st century. *Science*, **326**, 123–125.

Rayner, P. J., 2021: Atmospheric inversions of greenhouse gas fluxes: A story of uneven development, abstract id: ACG34-01, *JpGU annual meeting*.

Ricaud, P., J.-L. Attié, R. Chalinel, F. Pasternak, J. Léonard, I. Pison, E. Pattey, R. L. Thompson, Z. Zelinger, J. Lelieveld, J. Sciare, N. Saitoh, J. Warner, A. Fortems-Cheiney, H. Reynal, J. Vidot, L. Brooker, L. Berdeu, O. Saint-Pé, P. K. Patra, M. Dostál, J. Suchánek, V. Nevrlý, and C. G. Zwaaftink, 2021: The Monitoring Nitrous Oxide Sources (MIN_2OS) satellite project.

Remote Sens. Environ., **266**, 112688, doi:10.1016/j.rse.2021.112688.

Saikawa, E., R. G. Prinn, E. Dlugokencky, K. Ishijima, G. S. Dutton, B. D. Hall, R. Langenfelds, Y. Tohjima, T. Machida, M. Manizza, M. Rigby, S. O'Doherty, P. K. Patra, C. M. Harth, R. F. Weiss, P. B. Krummel, M. van der Schoot, P. J. Fraser, L. P. Steele, S. Aoki, T. Nakazawa, and J. W. Elkins, 2014: Global and regional emissions estimates for N_2O. *Atmos. Chem. Phys.*, **14**, 4617–4641.

Sander, S. P., R. R. Friedl, J. P. D. Abbatt, J. R. Barker, J. B. Burkholder, D. M. Golden, C. E. Kolb, M. J. Kurylo, G. K. Moortgat, P. H. Wine, R. E. Hule, and V. L. Orkin, 2011: *Chemical Kinetics and Photochemical Data for Use in Atmospheric Studies, Evaluation No. 17*. JPL Publication 10-6, Jet Propulsion Laboratory, Pasadena, 684 pp.

Santoni, G. W., B. C. Daube, E. A. Kort, R. Jiménez, S. Park, J. V. Pittman, E. Gottlieb, B. Xiang, M. S. Zahniser, D. D. Nelson, J. B. McManus, J. Peischl, T. B. Ryerson, J. S. Holloway, A. E. Andrews, C. Sweeney, B. Hall, E. J. Hintsa, F. L. Moore, J. W. Elkins, D. F. Hurst, B. B. Stephens, J. Bent, and S. C. Wofsy, 2014: Evaluation of the airborne quantum cascade laser spectrometer (QCLS) measurements of the carbon and greenhouse gas suite – CO_2, CH_4, N_2O, and CO – During the CalNex and HIPPO campaigns. *Atmos. Meas. Tech.*, **7**, 1509–1526.

Sekiguchi, M., and T. Nakajima, 2008: A k-distribution-based radiation code and its computational optimization for an atmospheric general circulation model. *J. Quant. Spectrosc. Radiat. Transfer*, **109**, 2779–2793.

Solazzo, E., M. Crippa, D. Guizzardi, M. Muntean, M. Choulga, and G. Janssens-Maenhout, 2021: Uncertainties in the Emissions Database for Global Atmospheric Research (EDGAR) emission inventory of greenhouse gases. *Atmos. Chem. Phys.*, **21**, 5655–5683.

Takigawa, M., M. Takahashi, and H. Akiyoshi, 1999: Simulation of ozone and other chemical species using a Center for Climate System Research/National Institute for Environmental Studies Atmospheric GCM with coupled stratospheric chemistry. *J. Geophys. Res.*, **104**, 14003–18.

Thompson, R. L., F. Chevallier, A. M. Crotwell, G. Dutton, R. L. Langenfelds, R. G. Prinn, R. F. Weiss, Y. Tohjima, T. Nakazawa, P. B. Krummel, L. P. Steele, P. Fraser, S. O'Doherty, K. Ishijima, and S. Aoki, 2014a: Nitrous oxide emissions 1999 to 2009 from a global atmospheric inversion. *Atmos. Chem. Phys.*, **14**, 1801–1817.

Thompson, R. L., K. Ishijima, E. Saikawa, M. Corazza, U. Karstens, P. K. Patra, P. Bergamaschi, F. Chevallier, E. Dlugokencky, R. G. Prinn, R. F. Weiss, S. O'Doherty, P. J. Fraser, L. P. Steele, P. B. Krummel, A. Vermeulen, Y. Tohjima, A. Jordan, L. Haszpra, M. Steinbacher, S.

Van der Laan, T. Aalto, F. Meinhardt, M. E. Popa, J. Moncrieff, and P. Bousquet, 2014b: TransCom N_2O model inter-comparison – Part 2: Atmospheric inversion estimates of N_2O emissions. *Atmos. Chem. Phys.*, **14**, 6177–6194.

Thompson, R. L., P. K. Patra, K. Ishijima, E. Saikawa, M. Corazza, U. Karstens, C. Wilson, P. Bergamaschi, E. Dlugokencky, C. Sweeney, R. G. Prinn, R. F. Weiss, S. O'Doherty, P. J. Fraser, L. P. Steele, P. B. Krummel, M. Saunois, M. Chipperfield, and P. Bousquet, 2014c: TransCom N_2O model inter-comparison – Part 1: Assessing the influence of transport and surface fluxes on tropospheric N_2O variability. *Atmos. Chem. Phys.*, **14**, 4349–4368.

Thompson, R. L., L. Lassaletta, P. K. Patra, C. Wilson, K. C. Wells, A. Gressent, E. N. Koffi, M. P. Chipperfield, W. Winiwarter, E. A. Davidson, H. Tian, and J. G. Canadell, 2019: Acceleration of global N_2O emissions seen from two decades of atmospheric inversion. *Nat. Climate Change*, **9**, 993–998.

Tian, H., R. Xu, J. G. Canadell, R. L. Thompson, W. Winiwarter, P. Suntharalingam, E. A. Davidson, P. Ciais, R. B. Jackson, G. Janssens-Maenhout, M. J. Prather, P. Regnier, N. Pan, S. Pan, G. P. Peters, H. Shi, F. N. Tubiello, S. Zaehle, F. Zhou, A. Arneth, G. Battaglia, S. Berthet, L. Bopp, A. F. Bouwman, E. T. Buitenhuis, J. Chang, M. P. Chipperfield, S. R. S. Dangal, E. Dlugokencky, J. W. Elkins, B. D. Eyre, B. Fu, B. Hall, A. Ito, F. Joos, P. B. Krummel, A. Landolfi, G. G. Laruelle, R. Lauerwald, W. Li, S. Lienert, T. Maavara, M. MacLeod, D. B. Millet, S. Olin, P. K. Patra, R. G. Prinn, P. A. Raymond, D. J. Ruiz, G. R. van der Werf, N. Vuichard, J. Wang, R. F. Weiss, K. C. Wells, C. Wilson, J. Yang, and Y. Yao, 2020: A comprehensive quantification of global nitrous oxide sources and sinks. *Nature*, **586**, 248–256.

Tohjima, Y., H. Mukai, S. Maksyutov, Y. Takahashi, T. Machida, M. Katsumoto, and Y. Fujinuma, 2000: Variations in atmospheric nitrous oxide observed at Hateruma monitoring station. *Chemosphere*, **2**, 435–443.

Wang, C., B. Amon, K. Schulz, and B. Mehdi, 2021: Factors that influence nitrous oxide emissions from agricultural soils as well as their representation in simulation models: A review. *Agronomy*, **11**, 770, doi:10.3390/agronomy11040770.

Wanninkhof, R., 1992: Relationship between wind speed and gas exchange over the ocean. *J. Geophys. Res.*, **97**, 7373–7382.

Watanabe, S., T. Hajima, K. Sudo, T. Nagashima, T. Takemura, H. Okajima, T. Nozawa, H. Kawase, M. Abe, T. Yokohata, T. Ise, H. Sato, E. Kato, K. Takata, S. Emori, and M. Kawamiya, 2011: MIROC-ESM 2010: Model description and basic results of CMIP5-20c3m experiments. *Geosci. Model Dev.*, **4**, 845–872.

Wilson, C., M. P. Chipperfield, M. Gloor, and F. Chevallier, 2014: Development of a variational flux inversion system (INVICAT v1.0) using the TOMCAT chemical transport model. *Geosci. Model Dev.*, **7**, 2485–2500.

Winiwarter, W., L. Höglund-Isaksson, Z. Klimont, W. Schöpp, and M. Amann, 2018: Technical opportunities to reduce global anthropogenic emissions of nitrous oxide. *Environ. Res. Lett.*, **13**, 014011, doi:10.1088/1748-9326/aa9ec9.

Wofsy, S. C., 2011: HIAPER Pole-to-Pole Observations (HIPPO): Fine-grained, global-scale measurements of climatically important atmospheric gases and aerosols. *Philos. Trans. Roy. Soc. London, Ser. A*, **369**, 2073–2086.

Wolter, K., and M. S. Timlin, 2011: El Niño/Southern Oscillation behaviour since 1871 as diagnosed in an extended multivariate ENSO index (MEI.ext). *Int. J. Climatol.*, **31**, 1074–1087.

Yang, S., B. X. Chang, M. J. Warner, T. S. Weber, A. M. Bourbonnais, A. E. Santoro, A. Kock, R. E. Sonnerup, J. L. Bullister, S. T. Wilson, and D. Bianchi, 2020: Global reconstruction reduces the uncertainty of oceanic nitrous oxide emissions and reveals a vigorous seasonal cycle. *Proc. Natl. Acad. Sci. U.S.A. (PNAS)*, **117**, 11954–11960.

Yoshida, N., H. Morimoto, M. Hirano, I. Koike, S. Matsuo, E. Wada, T. Saino, and A. Hattori, 1989: Nitrification rates and ^{15}N abundances of N_2O and NO_3^- in the western North Pacific. *Nature*, **342**, 895–897.